Entanglement spectrum and Wannier center flow of the Hofstadter problem

Zhoushen Huang and Daniel P. Arovas

Phys. Rev. B **86**, 245109 — Published 12 December 2012

DOI: 10.1103/PhysRevB.86.245109

Entanglement spectrum and Wannier center flow of the Hofstadter problem

Zhoushen Huang and Daniel P. Arovas
Department of Physics, University of California at San Diego, La Jolla CA 92093
(Dated: November 26, 2012)

We examine the quantum entanglement spectra and Wannier functions of the square lattice Hofstadter model. Consistent with previous work on entanglement spectra of topological band structures, we find that the entanglement levels exhibit a spectral flow similar to that of the full system's energy spectrum. While the energy spectra are continuous, with cylindrical boundary conditions the entanglement spectra exhibit discontinuities associated with the passage of an energy edge state through the Fermi level. We show how the entanglement spectrum can be understood by examining the band projectors of the full system and their behavior under adiabatic pumping. In so doing we make connections with the original TKNN work[1] on topological two-dimensional band structures and their Chern numbers. Finally we consider Wannier states and their adiabatic flows, and draw connections to the entanglement properties.

PACS numbers: 73.43.Cd

1. INTRODUCTION

In the presence of a uniform magnetic field, the energy spectrum of a noninteracting two-dimensional electron gas is arranged in discrete, equally spaced Landau levels. The Hall conductivity of n filled Landau levels is $\sigma_{xy} = ne^2/h$. A discretized version of this model, due to Hofstadter[2], has electrons hopping on a two-dimensional lattice with complex tight-binding amplitudes $t_{ij} = t\, e^{iA_{ij}}$, such that the magnetic flux through each unit cell is a rational multiple p/q of the Dirac flux quantum. The gauge field A_{ij} can be made periodic by choosing a magnetic unit cell comprising q structural unit cells of the lattice. For a lattice with an r element basis, this results in qr energy subbands which in general do not cross, a consequence of the Wigner-von Neumann theorem; the continuum limit is recovered at low energies for $q \to \infty$. Plotting these energies as a function of $\phi \equiv 2\pi p/q$ yields the famous 'Hofstadter butterfly'. As shown in a seminal paper by Thouless *et al.*[1] (TKNN), to each band index j there corresponds an integer Chern number C_j, which physically represents the contribution to the Hall conductivity when band j is filled. The main differences with respect to the continuum are (i) the tight-binding subbands are dispersive, and (ii) whereas $C_j = 1$ for each Landau level in the continuum, the Chern indices of the TKNN bands are in general nonuniform.

The Chern number is an integer invariant which reflects aspects of the bulk band topology. As such it is robust and invariant with respect to parameter variations which do not collapse the band gaps. The nontrivial bulk topology is also manifested at the edge. Hatsugai[3] showed that the number of edge modes interpolating between bulk bands separated by a gap is equal to the sum of the Chern indices of all bands below that gap. The spectral flow of the edge energy levels as a function of the momentum parallel to the edge is also reflected in the behavior of the quantum entanglement spectrum[4,5] of the many-body reduced density matrix obtained by partitioning the system along a translationally-invariant boundary. For noninteracting fermions, the spectrum of the reduced density matrix itself corresponds to that of a noninteracting 'entanglement Hamiltonian' determined by the one-body correlation matrix of the original system[6–9]. However there are also exceptions to the edge-entanglement correspondence. For example, the entanglement spectrum has protected midgap modes for a system with inversion symmetry even if the edge modes are gapped[10,11]. In certain cases, one also has to tune the boundary conditions for a system with nontrivial topology in order for its energy edge modes to be gapless[12], while such tuning is not required to observe the entanglement spectral flow. Thus in certain sense, the entanglement spectrum is a more robust test of the bulk topology.

Once one specifies the wavevector $\vec{k}_\perp$ along the translationally invariant partition boundary, the entanglement Hamiltonian becomes effectively one-dimensional, and the localization properties of such states can be considered from the perspective of a Wannier basis[13], and several recent studies of topological insulators have invoked Wannier states[14,15] in their analyses. While nonvanishing Chern numbers provide an obstruction which rules out exponentially localized Wannier states in higher dimensions[16], the one-dimensional entanglement eigenstates at fixed $\vec{k}_\perp$ can be so localized, and for topologically nontrivial bulk band topologies, their Wannier centers exhibit a spectral flow similar to that observed in the edge and entanglement spectra.

In this paper, we investigate the spectral flow of entanglement levels and Wannier states derived from the two-dimensional square lattice Hofstadter model. We identify the correspondence between these flows and the Chern numbers of the bulk bands, and investigate the effect of adiabatic pumping on the wavefunctions of different energy bands of the system. We consider both energy eigenstates as well as 'entanglement eigenstates' of the corresponding reduced density matrix which results from a spatial partitioning of the system into two parts.

2. HOFSTADTER MODEL AND ITS ENTANGLEMENT SPECTRUM

2.1. Hofstadter model

The Hofstadter model[2] is a discrete model of electrons in two space dimensions and in the presence of magnetic flux. It is defined by a lattice tight-binding Hamiltonian,

$$\hat{H} = -\sum_{\langle ij \rangle} \left[t_{ij}\, c_i^\dagger c_j + \text{H.c.} \right] , \tag{1}$$

where $t_{ij} = |t_{ij}|\, e^{iA_{ij}}$ is the complex hopping amplitude between sites i and j. The $\mathsf{U}(1)$ flux ϕ_p through a plaquette p is the product $\prod_{\partial p} e^{iA_{ij}}$ over a counterclockwise path of links along its boundary, ∂p. We shall only consider the case of uniform amplitude hopping, *i.e.* $|t_{ij}| = 1$.

In the continuum limit, energy eigenstates of ballistic electrons collapse into macroscopically degenerate, equally spaced Landau levels. The degeneracy of each Landau level is $N_{\rm L} = B\Omega/\phi_0$, where B is the magnetic field, Ω the total area covered by the system, and $\phi_0 = hc/e$ is the Dirac flux quantum. The spectral flow of entanglement eigenstates in this limit was investigated by Rodríguez and Sierra[17]. On the lattice, the Landau levels are no longer degenerate, but form magnetic subbands, each subband accommodating $N_{\rm L}$ states. The model may be defined on any lattice, but for definiteness we consider the square lattice. Our principal results do not depend qualitatively on the underlying lattice structure. (See Appendix B for the case of triangular lattice.)

As is well-known, while ϕ_p is periodic on the scale of the structural unit cell, the vector potential A_{ij} is not. However, if the flux ϕ per plaquette is uniform and is 2π times a rational number p/q, a gauge can be chosen where A_{ij} is periodic on the scale of a 'magnetic unit cell' comprising q elementary structural cells. For example, one can choose

$$A_{ij} = \phi\, y_i\, \delta_{x_i, x_j+1}\, \delta_{y_i, y_j} , \tag{2}$$

where (x_i, y_i) are integer coordinates for lattice site i. The magnetic unit cell is then a $1\times q$ tower of lattice cells, and one obtains a $q\times q$ Hamiltonian matrix with nonzero matrix elements $H_{n,n} = -2\cos(k_x + n\phi)$, $H_{n,n+1} = -1$, $H_{N,1} = -e^{ik_y}$, and remaining elements determined by hermiticity. This results in q magnetic subbands with dispersion $\varepsilon_a(k_x, k_y)$. Here we are concerned with entanglement spectra, and to this end we consider a cylinder with periodic boundary conditions in the x-direction and N_y sites in the y-direction. The Hamiltonian matrix is

$$H(k_x, N_y, z) = -\begin{pmatrix} 2\cos(k_x+\phi) & 1 & 0 & \cdots & z^* \\ 1 & 2\cos(k_x+2\phi) & 1 & & 0 \\ 0 & 1 & \ddots & & \vdots \\ \vdots & & & & 1 \\ z & 0 & \cdots & 1 & 2\cos(k_x+N_y\phi) \end{pmatrix} . \tag{3}$$

Here, k_x is the Bloch phase in the x direction, N_y is the number of lattice sites in the y direction, and z controls the boundary condition on y: $z = 0$ for cylindrical boundary conditions (*i.e.* periodic in the x-direction and open in the y-direction), $z = 1$ with $N_y \bmod q = 0$ for periodic boundary conditions; unimodular complex z can be interpreted as flux threading the compactified cylinder. Note that for $z \in \mathbb{R}$ the Hamiltonian is real and hence the eigenfunctions may be chosen to be real as well.

In what follows, we focus on the case with integer number K_y of magnetic unit cells in the y direction ($N_y = qK_y$), which is more convenient for switching between open and periodic boundary. In ref. 3, the edge solution is derived with the requirement of commensurability, *i.e.*, $N_y = qK_y - 1$, in order to exploit some structure in the transfer matrix formalism. This restriction can be lifted in the thermodynamic limit $N_y \to \infty$, where the spectrum of edge states localized at $y = 1$ is unchanged, while that of states localized at $y = N_y$ is shifted in k_x. A proof is given in Appendix A.

2.2. Entanglement spectrum

Imagine partitioning the sites of our lattice into two groups, A and B. If a many-body wavefunction $|\Psi\rangle$ can be written as a direct product $|\Psi^{\rm A}\rangle \otimes |\Psi^{\rm B}\rangle$, the wavefunction is said to be unentangled with respect to this partition. More generally, let $\varrho = |\Psi\rangle\langle\Psi|$ be the projector onto $|\Psi\rangle$. Tracing out over the B sites yields the reduced density matrix $\tilde{\varrho} = \mathsf{Tr}_{\rm B}\, \varrho$, whose eigenvalues constitute the entanglement spectrum[4]. The von Neumann entropy, $S = -\mathsf{Tr}\, \tilde{\varrho} \ln \tilde{\varrho}$, provides a measure of the degree of entanglement.

If the boundary between A and B is irregular, then translational invariance is completely broken, but if the boundary is such that the A region remains periodic in

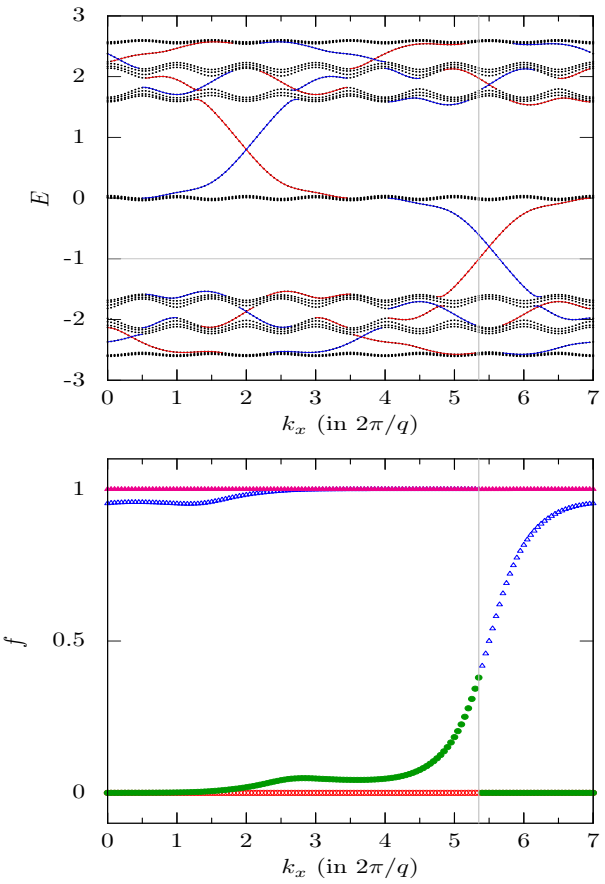

FIG. 1: (Color online) Energy levels (top) and entanglement occupancies (bottom) for the square lattice Hofstadter model with flux $p/q = 3/7$ per plaquette, on a cylinder of height $N_y = 28$ as a function of the conserved crystal momentum k_x. The Fermi level E_F lies inside the third gap (grey line), and the occupied bands below E_F contribute a total Chern number $C_{\rm occ} = 1$. The energy spectrum (top) is shown for cylindrical boundary conditions, with the black dots indicating bulk levels, the red lines indicating edge levels localized along the lower edge ($y = 1$), and the blue lines indicating edge levels localized along the upper edge ($y = N_y = 28$). The vertical gray line marks the value of k_x where the lower edge mode crosses the Fermi level. The entanglement occupancies f_a (bottom) are computed for the lower half of the cylinder ($1 \le y \le 14$), color and symbol-coded according to a. Although the overall flow appears continuous, there is a discontinuity in the occupancies $f_a(k_x)$ where the lower edge mode crosses E_F, resulting in a sudden color change in the plot.

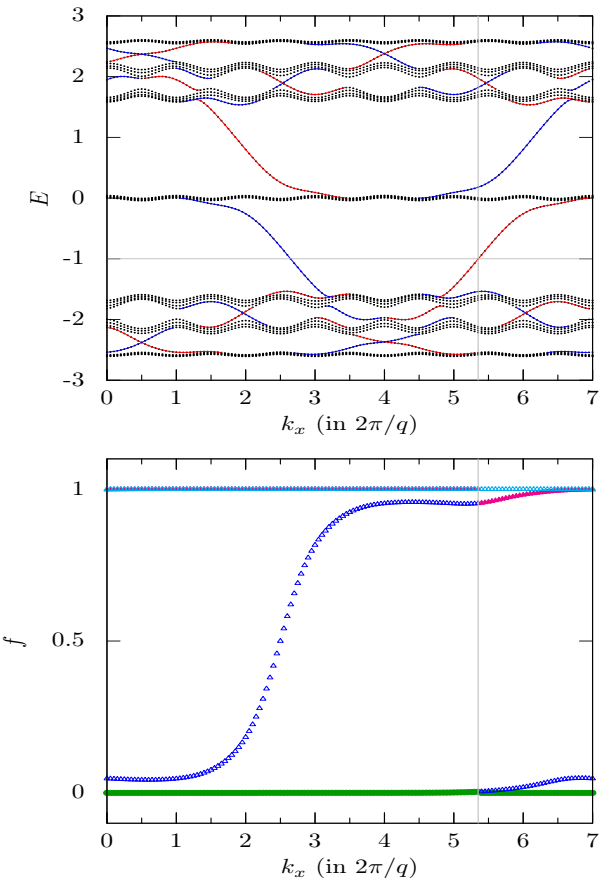

FIG. 2: (Color online) Same as in Fig. 1 but with $N_y = 29$ and $M = 15$.

one direction (or more than one, in the case of systems in more than two space dimensions), then the eigenstates of $\tilde{\varrho}$ can be classified by a corresponding crystal momentum, and one can investigate the spectral flow of the entanglement levels[5].

2.2.1. The correlation matrix method

A general recipe for computing the reduced density matrix for noninteracting Fermi systems has been derived by Cheong and Henley[6]. Let I and J denote sites in the full system, whose Hamiltonian is $\hat{H} = H_{IJ}\, c_I^\dagger c_J$. The statistics of this Hamiltonian are then completely determined by the one-body correlation matrix $\mathcal{G}_{IJ} = \langle c_I^\dagger c_J \rangle = \mathsf{Tr}\,(\varrho\, c_I^\dagger c_J)$, where ϱ is the density matrix. Now consider a bipartition of the full system into two subsystems A and B, and let i and j denote sites within A. Then $G_{ij} = \langle c_i^\dagger c_j \rangle = (R\mathcal{G}R^\mathsf{T})_{ij}$ where $R_{iI} = \delta_{iI}$ is an oblong matrix of dimensions $N_A \times (N_A + N_B)$ with 1's along the diagonal; $N_{A(B)}$ is the size of the $A(B)$ subspace. *I.e.* R spatially projects onto A. Thus G is a submatrix of $\mathcal{G}$, and a key fact, due to Peschel[9], is that we may write $G_{ij} = \mathsf{Tr}\,(\tilde{\varrho}\, c_i^\dagger c_j)$, where $\tilde{\varrho} = \exp(-\hat{K})/Z$ is the reduced density matrix (RDM) and $\hat{K} \equiv \Gamma_{ij}\, c_i^\dagger\, c_j$ is the dimensionless 'entanglement Hamiltonian' (both restricted to A). One then finds $G = \left\{\exp(\Gamma^\mathsf{T}) + 1\right\}^{-1}$, and the normalization Z follows from $\mathsf{Tr}\,(\tilde{\varrho}) = 1$. The

N_A eigenvalues $\{\gamma_a\}$ of $\Gamma^{\mathsf{T}} = \ln\left(G^{-1} - 1\right)$ are the entanglement 'quasienergies', and the eigenvalues of G are then Fermi functions of the quasienergies[7], *viz.*

$$f_a = \frac{1}{\exp(\gamma_a) + 1} \ . \tag{4}$$

For our system, the translation invariance along x means k_x is a good quantum number, and for each k_x, the system can be regarded as one-dimensional. Thus, $H_{IJ}(k_x)$ and $\mathcal{G}_{IJ}(k_x)$ are of dimension N_y, and I and J label rings and not single sites. In our study, the Fermi energy E_{F} is always placed within some bulk gap. For periodic boundary conditions, $\mathcal{G}$ is then a sum of projectors onto the occupied bands. With open boundaries, there will be edge modes which cross the Fermi level. In either case, we take the A subsystem to be the bottom part of the cylinder, with $y \in [1, M]$. Thus G is the upper left $M \times M$ block of $\mathcal{G}$.

2.2.2. *Rank of G and $\mathbf{1} - G$*

The eigenvalues of G may contain *exact* zeros or ones. The number of zeros and ones, denoted as D_0 and D_1 respectively, are by definition the dimensions of the kernels of G and $\mathbf{1} - G$. If ν bulk bands are occupied with periodic boundary conditions, then the total rank of $\mathcal{G}(k_x)$ is $\nu N_y/q$, since each of the q bands contains an equal number of states. Thus if $M \geq \nu N_y/q$, the rank of G will also be $\nu N_y/q$. For $M \leq \nu N_y/q$, the rank of G is M. Thus,

$$\mathrm{rank}(G) = \min(M, \nu N_y/q) \ , \tag{5}$$
$$D_0 = M - \mathrm{rank}(G) \ , \tag{6}$$

and similarly

$$\mathrm{rank}(\mathbf{1} - G) = \min\Big\{M, N_y(1 - \nu/q)\Big\} \ , \tag{7}$$
$$D_1 = M - \mathrm{rank}(\mathbf{1} - G) \ , \tag{8}$$

where $N_y(1-\nu/q)$ is the rank of $\mathbf{1}-\mathcal{G}$, the projector onto unoccupied bands.

As we shall see, with cylindrical boundary conditions, the rank of $\mathcal{G}$ changes with k_x whenever an edge state crosses the Fermi level. As a result, D_0 and/or D_1 are discontinuous at such k_x values for certain range of M. It is easy to verify that the condition for $D_0 = D_1 = 0$ is $M \leq \min(\nu/q, 1 - \nu/q) \times N_y$.

2.2.3. *Entanglement occupancy, quasienergy, and spectral flow*

Fig. 1 shows the energy spectrum and entanglement occupancy for $p/q = 3/7$, $N_y = 28$, and $M = 14$, using cylindrical boundary conditions. The Fermi energy E_{F} lies within the third gap. The total Chern number of the three occupied bands is $C_{\mathrm{occ}} = \sum_{j=1}^{3} C_j = 1$, which is also the number of times the lower edge mode, localized at $y = 1$ (the red line in the plot), flows across the gap, *i.e.*, the winding number[3]. The sign of C_{occ} is reflected in the direction of the edge flow, *e.g.* $C_{\mathrm{occ}} = -1$ for 4 filled bands, and the lower edge flows downward. Several features are noteworthy:

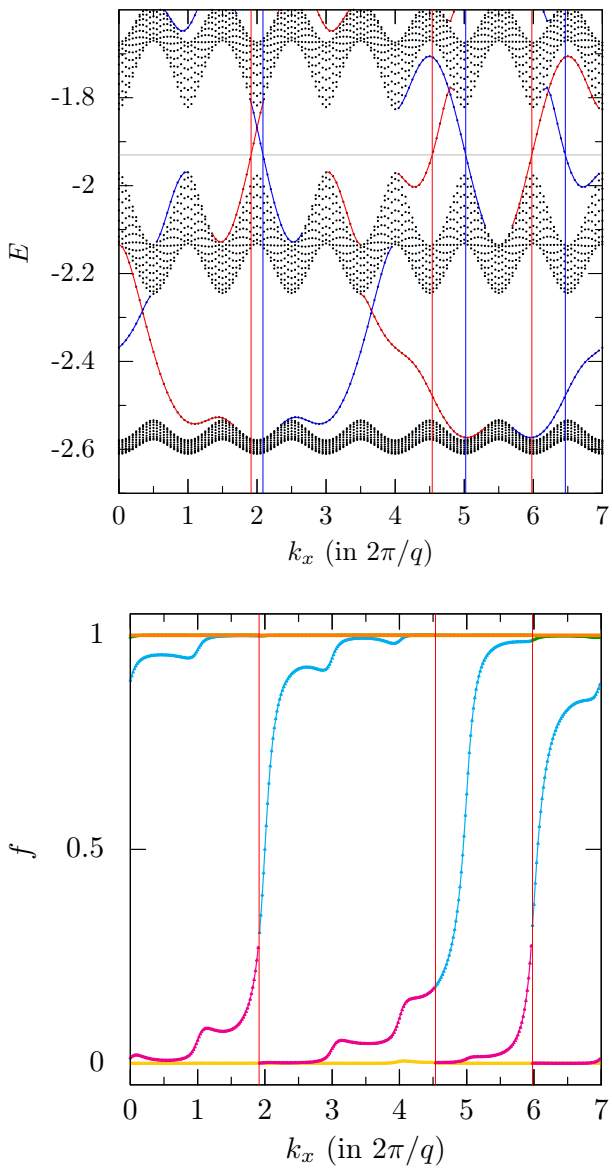

FIG. 3: (Color online) Hofstadter model with flux $p/q = 3/7$ per plaquette on a cylinder of height $N_y = 70$. Top: detail of energy spectrum showing lowest three energy bands. The Fermi level lies at $E_{\mathsf{F}} = -1.9$ (grey horizontal line). The total Chern number of the occupied bands is $C_{\mathrm{occ}} = 3$. Red (blue) vertical lines indicate k_x at which the lower (upper) edge modes cross the Fermi energy (k_x^{L} and k_x^{U} in text). Bottom: entanglement occupancies f_a after tracing out the upper half of the cylinder.

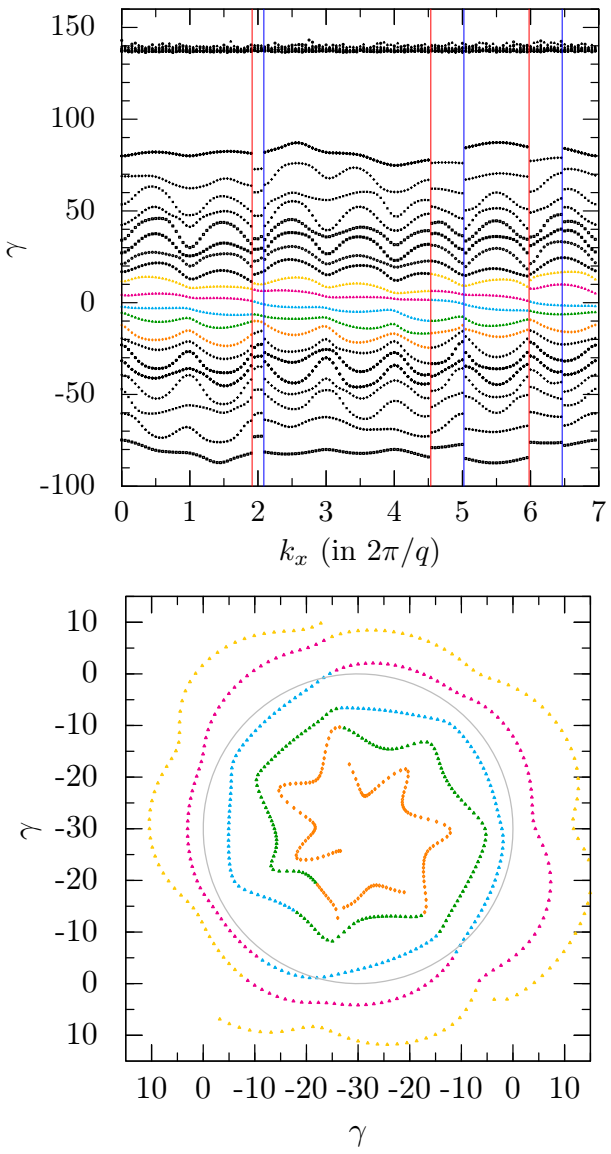

FIG. 4: (Color online) Same system as in Fig. 3. Top: entanglement quasi-energies γ_a. 20 levels are below the large 'gap' – the same as the number of occupied levels in the full system. Colored levels are also plotted in Fig. 3 with the same color scheme. Red and blue vertical lines mark the k_x values at which lower and upper edge modes of the cylindrical Hamiltonian are crossed by the Fermi level ($k_x^{\rm L}$ and $k_x^{\rm U}$ in text). Bottom: quasienergy in 2D polar coordinates. The radius is the quasienergy and the polar angle is k_x. The black circle corresponds to $\gamma = 0$. There are three curves spiraling outward in the clockwise direction, corresponding to total Chern number $C = 3$.

(a) Most levels are clustered near $f = 0$ and $f = 1$. This reflects the fact that $E_{\rm F}$ lies inside a bulk gap. Taking linear combinations of the occupied states in the full system, one can create wavefunctions which are mostly confined to either (A or B) subsystem. The same consideration applies to unoccupied states. In the thermodynamic limit, the fraction of occupied states in A and in B should be the same as that for the full system. This is confirmed by our numerical results. The entanglement eigenstates with $f \sim \frac{1}{2}$ are localized along $y \approx M$. As is the case for the edge modes of the full Hamiltonian, the number of entanglement levels flowing between $f \simeq 0$ and $f \simeq 1$ is the same as the total Chern number number $C_{\rm occ}$ of the filled bands. This is depicted in Fig. 1 for $C_{\rm occ} = 1$ and in Fig. 3(b) for $C_{\rm occ} = 3$.

(b) The occupancy $f_a(k_x)$ is discontinuous at $k_x = k_x^{\rm L}$, where the lower cylindrical boundary edge modes of $\hat{H}$ cross the Fermi level; these are the red curves in Fig. 3(a). For example, in Figs. 1 and 2, where entanglement levels with different indices a are plotted in different colors, the tenth (light blue) and eleventh (magenta) level occupancies are each discontinuous at $k_x^{\rm L}$, but satisfy $f_{a=10}(k_x^{\rm L}+0^+) = f_{a=11}(k_x^{\rm L}-0^+)$. The number of distinct such $k_x^{\rm L}$ values is the number of lower edge mode Fermi level crossings, which is $|C_{\rm occ}|$. Thus, as one increases k_x through each such crossing, the number of levels with $f \simeq 1$, and hence the total occupancy $\sum_a f_a$ of the A subsystem, drops discontinuously by unity due to the exclusion of the edge mode. Eventually the $f \simeq 1$ levels are repopulated due to the aforementioned spectral flow. In order to conserve the rank of $G(k_x)$ (in the case of $M > {\rm rank}(\mathcal{G})$, *cf.* eqn. 6) upon increasing k_x by 2π, then, there must be a discontinuous repopulation of the $f \simeq 0$ levels. This occurs when the upper cylindrical boundary edge modes cross $E_{\rm F}$ at $k_x = k_x^{\rm U}$; these are the blue curves in Fig. 3(a). As these modes have a vanishingly small projection onto the A subsystem in the thermodynamic limit, they lead to no discontinuity in the total occupancy of A. A similar analysis of the occupancy discontinuity has recently been given by Alexandradinata *et al.*[18]

(c) From the occupancy spectrum, one can invert the Fermi distribution (eqn. 4) to get the quasienergy spectrum $\{\gamma_a\}$. A quasienergy plot more clearly reveals entanglement spectrum near $f = 0$ and $f = 1$, where many levels are clustered. In Fig. 4(a) (and equivalently the polar plot Fig. 4(b)), some key features are apparent. First, a substantial number of levels are clustered at $\gamma \approx 140$ ($f \sim 10^{-60}$) and are separated from the remaining levels by a pronounced gap. Actually this is a numerical artifact and these levels all lie at $\gamma = \infty$. Recall the earlier result ${\rm rank}(G) = \min(M, \nu N_y/q)$ in eqn. 6 for a system with periodic boundary conditions. Here we have $p/q = 3/7$, $N_y = 70$, $M = 35$, and $\nu = 2$ since $E_{\rm F}$ is placed in the gap between the second and third bulk bands. Thus we would expect ${\rm rank}(G) = 20$, and since the row dimension of G is $M = 35$, there should be 15 levels with $f = 0$, corresponding to $\gamma = +\infty$. Had one looked at a system with more than half filling, one would find entanglement quasienergies clustering at $\gamma = -\infty$ instead, where the entanglement occupancy is exactly 1. These would correspond to the kernel of $1 - G$.

(d) Since our system has cylindrical boundary conditions, there are edge states, and there is a discontinu-

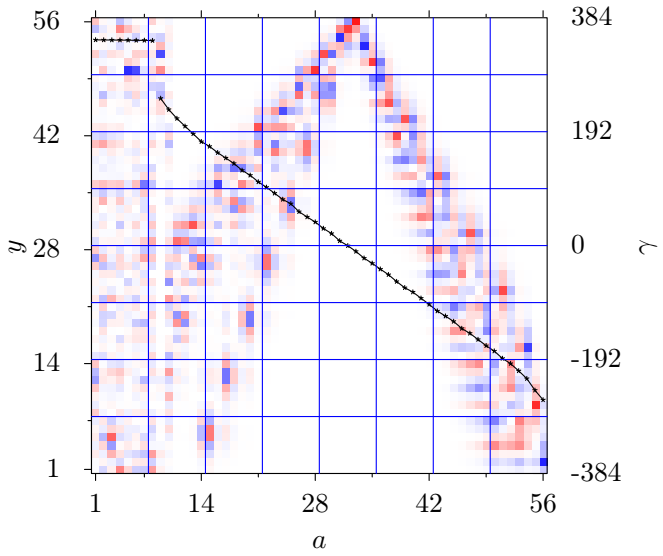

FIG. 5: (Color online) Normalized eigenfunctions $\tilde{\psi}_a(y)$ of G for $p/q = 3/7$, $N_y = 112$, $M = 56$, and $\nu = 3$ at $k_x = 2\pi/7$ (cylindrical boundary conditions). The Chern number of the filled bands is $C_{\rm occ} = 1$. Color corresponds to the sign of the wavefunction (red for positive, blue for negative), and intensity to amplitude (white for zero intensity). The black points are the entanglement energies γ_a.

ity in the quasienergy spectrum at each $k_x^{\rm L}$ and $k_x^{\rm U}$ value where lower and upper edge states are crossed by E_{F}. When both edge states lie below E_{F}, one counts 20 finite quasienergy levels. When k_x lies between consecutive $k_x^{\rm U}$ and $k_x^{\rm L}$ values, one of the lower boundary edge states has crossed the Fermi level, and the rank of G decreases to 19. The spectral flow in the vicinity of $\gamma \approx 0$ is continuous, however. Discontinuities in the entanglement energies occur for large values of $|\gamma|$, where the occupancy is close to 0 of 1. When an edge state passes from below E_{F} to above E_{F}, the rank of $\mathcal{G}$ changes discontinuously by -1. For increasing k_x, this occurs at any of the three $k_x^{\rm L}$ points in Fig. 3(a). Such an edge state has almost perfect projection onto the A subsystem, hence its depopulation leads to a sudden rearrangement of entanglement levels with large negative quasienergies γ_a ($f_a \approx 1$) and a loss of one such level. For $k_x = k_x^{\rm U}$, where the change $\Delta\,\mathrm{rank}(\mathcal{G}) = +1$, the 'extra' level enters via a discontinuous rearrangement of the levels with large positive quasienergies ($f_a \approx 0$). (The situation is reversed if E_{F} lies within the first gap, in which case $\Delta\,\mathrm{rank}(\mathcal{G}) = +1$ at each $k_x^{\rm L}$ and $\Delta\,\mathrm{rank}(\mathcal{G}) = -1$ at each $k_x^{\rm U}$.) We see this clearly in Fig. 4(a), where the number of finite γ levels changes from 20 to 19 when k_x lies between consecutive $k_x^{\rm L}$ and $k_x^{\rm U}$ values.

2.2.4. *Entanglement eigenfunctions*

In Fig. 5 we plot the eigenfunctions $\tilde{\psi}_a$ of $G(k_x = 2\pi/7)$ for a larger $p/q = 3/7$ system, with $N_y = 112$, $M = 56$, and $\nu = 3$ at $k_x = 2\pi/7$. The Chern number of the filled bands is $C_{\rm occ} = 1$. States with finite γ_a are spatially resolved. The rank of G is $\nu N_y/q = 48$, corresponding to states #9 through #56 in the plot. The dimension of the kernel of G is then $\mathsf{dim}(G) - \mathsf{rank}(G) = 8$. These states all have $f_a = 0$, *i.e.* $\gamma_a = +\infty$, which is rendered as the flat ceiling of the black curve in the figure. They form the speckled region in the left of the figure. Note that states with $\gamma_a \approx 0$ ($f \approx \frac{1}{2}$) are localized near the cut $y = M$, and that those with large γ_a are localized away from the cut. We shall return to this point later, toward the end of the paper, after we discuss Wannier center flows.

2.2.5. *Effect of changing M*

Since the magnetic unit cell is set along the y-direction, N_y and M must be chosen as integer multiples of q if there are to be an integer number of unit cells in the full system and/or the lower (A) subsystem, respectively. As shown in Appendix A, changing N_y to $N_y + m$ ($m \in \mathbb{Z}$) keeps the lower edge modes intact, but shifts the k_x values for the upper edge modes by $-2\pi mp/q$. For example, the lower edge modes (red lines) are the same in Figs. 1 and 2, but the upper edge modes (blue lines) in Fig. 2 are shifted in k_x by $-6\pi/7$ relative to those in Fig. 1.

It turns out that changing M affects the entanglement occupancy in the same way as changing N_y would affect the edge modes. This is shown in the bottom rows of Figs. 1 and 2. We should mention that keeping M fixed while changing N_y will not change the occupancy spectrum in any appreciable way because that only shifts the upper edge modes. Changing N_y will thus change the $k_x^{\rm U}$ values, and consequently where the rearrangements of the $f \approx 0$ parts of the entanglement spectrum occur, but will not affect the spectral flow for $\gamma \approx 0$. The reason will become more clear in the next section.

3. ADIABATIC PUMPING OF BAND PROJECTORS

The entanglement level occupancies f_a are eigenvalues of the restricted correlation matrix $G = R\mathcal{G}R^{\mathsf{T}}$. In searching for an intuitive picture of the various features of the entanglement spectrum, it is then natural to examine the unrestricted projector $\mathcal{G}$. We found that much information can be extracted from $\mathcal{G}$ itself.

In this section, we will use periodic boundary condition in the y-direction, *i.e.* $z = 1$ and $N_y \bmod q = 0$ in eqn. 3. The Hamiltonian of eqn. 3 then satisfies

$$H(k_x + \phi) = T_y^\dagger\, H(k_x)\, T_y \ , \qquad (9)$$

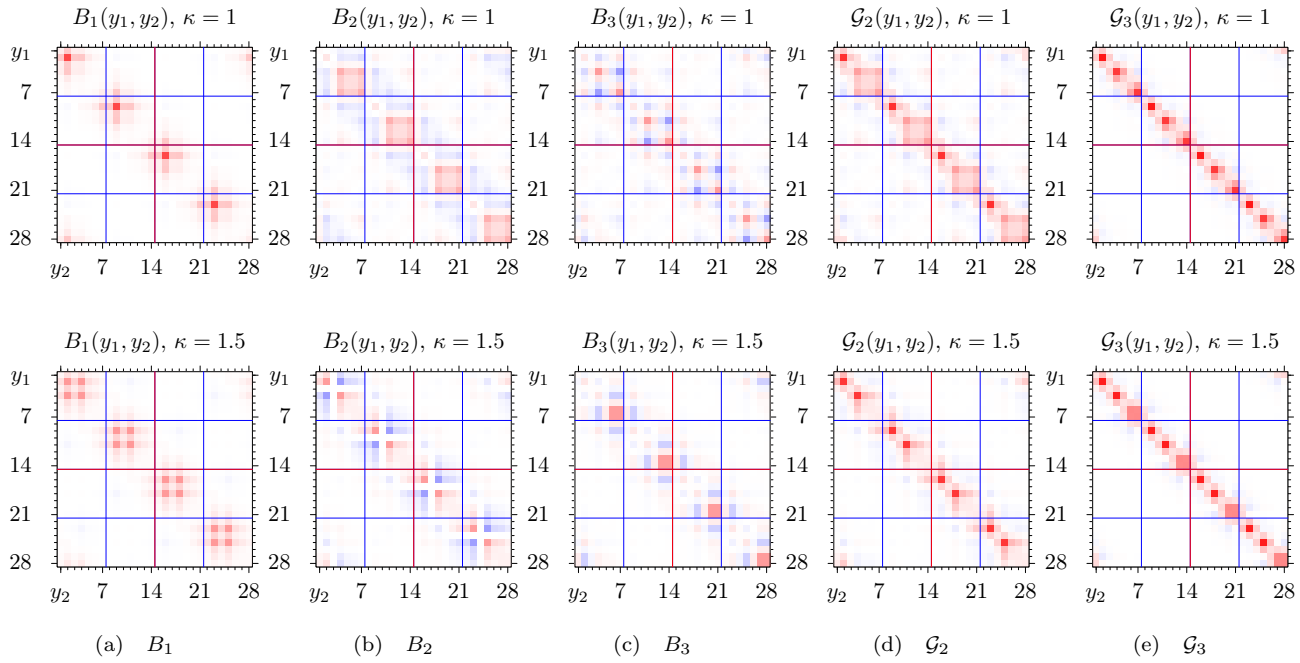

FIG. 6: (Color online) Full system band projectors for $p/q = 3/7$, $N_y = 28$, with periodic boundary conditions in y and $k_x = 2\pi\kappa/q$. B_j is the projector onto the j^{th} band, and $\mathcal{G}_\nu = B_1 + \ldots + B_\nu$ the projector onto the lowest ν bands. The magnitude of the matrix elements are represented by intensity and their sign by color (red positive, blue negative, white zero). y_1 and y_2 are the row and column indices of the projectors. Blue rules mark boundary of the magnetic unit cells. Red rules mark the bipartite cut, so the top-left quadrant of $\mathcal{G}$ corresponds to the restricted correlation matrix G. Only $\kappa = 1$ and $3/2$ are shown here due to space restriction. Corresponding plots for other κ values can be inferred from those shown here after shifting all matrix elements along the diagonal by t as the solution of eqn. 16. Similarly, projectors of all half odd-integer κ are obtained by shifting those of $\kappa = 3/2$. As k_x is increased from 0 to 2π (κ from 0 to q), the adiabatic pumping is evident in the diagonal motion of all matrix elements of the projectors. Note in particular that at integer κ, each diagonal block of $\mathcal{G}_3$ consists of three sharply localized packets: the top-left one is contributed by B_1, whereas the rest two result from the constructive addition of the diagonal blocks of B_2 and B_3. Similarly, at half odd-integer κ, B_1 and B_2 add constructively, yielding the two sharp packets in each diagonal block of $\mathcal{G}_2$. The Chern number corresponds to how many magnetic unit cell boundaries (blue and red rules) any diagonal matrix element has passed by in one pumping period. Equivalently, it is the sum of diagonal matrix elements which are transferred across any magnetic unit cell boundary in one pumping period. For the $\mathcal{G}_\nu$ type, it is intuitively how many packets are transferred.

where $\phi = 2\pi p/q$ as before and where T_y is the translation operator by one lattice spacing in the y-direction:

$$T_y = \begin{pmatrix} \mathbf{0} & 1 \\ \mathbf{1}_{N_y-1} & \mathbf{0} \end{pmatrix} . \tag{10}$$

The unitarity of T_y guarantees that the bulk bands repeat themselves for q times over the interval $k_x \in [0, 2\pi]$. With each successive increase of k_x by $2\pi p/q$, the spectrum repeats and the corresponding energy eigenstates are shifted by $\Delta y = 1$. Denoting $B_j(k_x)$ as the projector onto the j^{th} band, we have that $\mathcal{G}(k_x) \equiv \mathcal{G}_\nu(k_x)$ is the projector onto the lowest ν filled bands,

$$\mathcal{G}_\nu(k_x) = \sum_{j=1}^{\nu} B_j(k_x) . \tag{11}$$

The covariance in k_x and y is reflected as

$$B_j(k_x + \phi\,;\, y_1\,,\, y_2) = B_j(k_x\,;\, y_1 + 1\,,\, y_2 + 1) , \tag{12}$$

where y_1 and y_2 are row and column indices for $B_j(k_x)$. Translational invariance on a scale of the magnetic unit cell corresponds to

$$B_j(k_x\,;\, y_1\,,\, y_2) = B_j(k_x\,;\, y_1 + q\,,\, y_2 + q) \tag{13}$$

The same relations hold for $\mathcal{G}_\nu$.

While these projectors are explicitly constructed using the Bloch states, which are spatially extended, the fact that their eigenvalues are degenerate (either 0 or 1) means one may construct localized eigenstates around the cylinder, for each k_x, by recombining Bloch states of different k_y with the same eigenvalue. In the continuum limit, where $q \to \infty$ with p finite, these correspond to the familiar Landau strip basis. In fact, the projectors themselves are localized: An illustration is provided in Fig. 6, which shows several B_j and $\mathcal{G}_\nu$ for $p/q = 3/7$ at $k_x = 2\pi\kappa/q$ for $\kappa = 1$ and $\kappa = 3/2$, both of which are local extrema of the energy bands. The size of the magnetic unit cell naturally divides the projectors into blocks

of size $q \times q$. It is not surprising that the off-diagonal blocks drop exponentially, a consequence of the analyticity of B_j in complex k_y[19]. What is perhaps unexpected is that at band troughs (integer κ for odd j and half-odd-integer κ for even j in Fig. 6), the projectors B_j, and especially $\mathcal{G}_\nu$, are quite well-localized even within the diagonal blocks. The diagonal matrix elements of the projectors correspond to electron density at the corresponding y coordinate. For single bands (B_j), any q consecutive diagonal elements sum to 1, thus one may think of them as constituting a wavepacket, and the projector B_j as consisting of N_y/q such wavepackets (one per magnetic unit cell). For each wavepacket, the weight is dominated by one or two elements, as one can see in Fig. 6. The localization of the projector sums $\mathcal{G}_\nu$ is even more prominent: when the gap between two neighboring bands is at a minimum, their projectors add constructively, resulting in two sharply localized dots on the diagonal line of $\mathcal{G}_\nu$. For example, in Fig. 6, B_2 and B_3 add constructively at $\kappa = 1$, yielding the lower two dots in each diagonal block of $\mathcal{G}_3$, and similarly, B_1 and B_2 add up to $\mathcal{G}_2$ for $\kappa = 3/2$. Now, q consecutive diagonal elements in $\mathcal{G}_\nu$ must sum to ν, thus each of the ν dots can be intuitively understood as one localized wavepacket. The constructive superposition of neighboring bands then indicates the corresponding single-band wavepackets have opposite parity so that the off-diagonal elements cancel each other. To relate to the aforementioned "strip" states, we note that any column of a projector is an eigenstate of the same projector, with eigenvalue 1[27]. The diagonal nature of these band projectors thus ensures the existence of such strip states.

We now establish a connection between the band projectors and the seminal work of Thouless *et al.*[1] on the Chern numbers for the Hofstadter bands. Consider first the individual band projectors B_j. We write

$$y = q\ell + m \quad , \quad k_x = \frac{2\pi\kappa}{q} \ , \tag{14}$$

where ℓ and m are integers. Thus ℓ is the magnetic unit cell coordinate, and m the coordinate within each such cell. For a single band, denote the position of any of its wavepackets as $m(\kappa)$, then (k_x, y) covariance implies

$$m(\kappa + tp) = m(\kappa) - t \quad , \quad t \in \mathbb{Z} \ . \tag{15}$$

Of course both m and κ are only defined *modulo* q. The relevant quantity in the k_x pumping is the 'velocity' of the packet (with k_x as 'time'), *i.e.*, the number of sites it traverses when κ is *effectively* increased by 1:

$$tp = sq + 1 \quad , \quad s \in \mathbb{Z} \ , \ |t| < q \ . \tag{16}$$

A graphical construction is shown in Fig. 7. Clearly, t will be the number of packets transported through any given boundary during the cycle $k_x \to k_x + 2\pi$ (number of blue flow lines in the figure). It is also equal to the number of magnetic cells traversed by a single packet. There is however a mod q ambiguity associated with the sign indeterminancy of t, *e.g.* for $p/q = 3/7$, one has

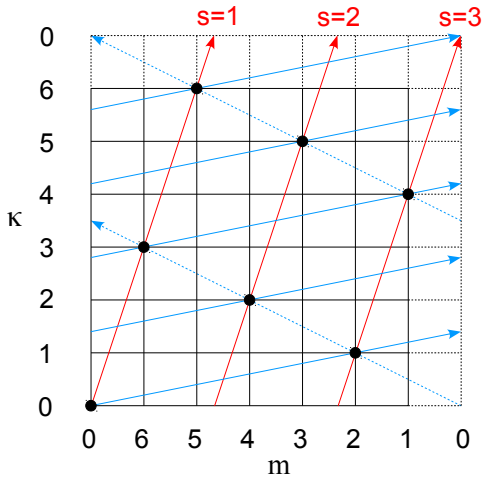

FIG. 7: (Color online) (m, κ) construction for $p/q = 3/7$, assuming $m = 0$ when $\kappa = 0$. Red line: flow in the order of T_y translation whereby $\kappa \to \kappa + p$ and $y \to y - 1$. Blue lines: flow in the order of k_x pumping. The number of time a packet is transferred across any boundary line, *e.g.* $m = 0$ line, is the same as the number of blue flow lines crossing the boundary line. There is a mod q ambiguity as can be seen from the validity of both the solid and dashed blue flows.

that $(t, s) = (5, 2)$ and $(-2, -1)$ both satisfy eqn. 16. In general, without looking at intermediate κ snapshots, one cannot tell if the packet had advanced by t or retreated by $q - t$. We have examined different p/q ratios on both square and triangular lattices, and we find that for the lowest band on a square lattice, the ambiguity can always be resolved, without needing to inspect intermediate κ, by picking the value of t which has the smaller magnitude $|t|$, *e.g.* $t = -2$ instead of 5 for B_1 in Fig. 6. Intuitively, this means the packet moves toward the nearest possible position allowed by eqn. 15.

Eqn. 16 is recognized as the Diophantine equation of TKNN[1] with $r = 1$, according to which t is simply C_1, the Chern number of the lowest band. The heuristic of taking the smaller $|C_1|$ in resolving the mod q ambiguity agrees with ref. 1. Since this picture does *not* distinguish between different bands, the Chern numbers of all bands are equivalent mod q.

The correlation matrix $\mathcal{G}_\nu$ for ν occupied bands has ν packets per diagonal block, with each moving according to eqn. 16, as required by the (k_x, y) covariance. However, their *collective* motion depends on their relative spacing. Consider for example the diagonal blocks of $\mathcal{G}_3$ for $\kappa = 1$, as shown in top right panel of Fig. 6. In each diagonal block, the diagonal elements with dominant weight (packets) are at $y = (2, 4, 7)$. Then (k_x, y) covariance requires that at $\kappa = 2$, they are moved to $y = (2 - t, 4 - t, 7 - t) = (4, 6, 9)$ where $t = -2$ is the solution to eqn. 16 as discussed before. Since $y = 9$ is simply the $y = 2$ element of the next diagonal block,

thus in each diagonal block, the packets of $\kappa = 2$ are at $y = (4, 6, 9 \text{ mod } 7 = 2)$. Comparing this with those of $\kappa = 1$, one can see that, effectively, only one packet moved from $y = 7$ to $y = 6$.

We found that for any $\nu \neq q$, this observation holds true (for $\nu = q$, $\mathcal{G}_\nu$ is identity). That is to say, as $\kappa \to \kappa + 1$, the net effect is for only *one* of the ν packets to change position. We will not attempt to explain this observation, but rather take it as a starting point, and explore its implications. Mathematically, this observation – the reduction of the motion of multiple wavepackets to that of a single mobile packet at a time – means that the positions of dominant diagonal elements (the packets) can be labeled in such a way that

$$m_i(\kappa + 1) = m_{i+1}(\kappa) \quad , \quad i = 1, 2, \ldots, \nu - 1 \tag{17}$$

with each m_i still satisfying eqn. 15, *i.e.* $m_i(\kappa + tp) = m_i(\kappa) - t$. Note that this does *not* mean m_i can be identified with the wavepacket of a single band: they result from constructive superposition of single-band projectors, as discussed earlier.

To illustrate eqn. 17, take again $\mathcal{G}_3$ as an example: at $\kappa = 1$, $(m_1, m_2, m_3) = (7, 2, 4)$, while at $\kappa = 2$, $(m_1, m_2, m_3) = (9 \text{ mod } 7 = 2, 4, 6)$. Then as κ increases by 1, the effective change is of one packet (the mobile one) moving from $m_1(\kappa)$ to $m_\nu(\kappa + 1)$ with stride t_ν,

$$m_\nu(\kappa + 1) = m_1(\kappa) - t_\nu \quad , \quad |t_\nu| < q \ . \tag{18}$$

The RHS is therefore $m_1(\kappa + t_\nu p)$, while the LHS is

$$m_\nu(\kappa + 1) = m_{\nu-1}(\kappa + 2) = \cdots = m_1(\kappa + \nu) \tag{19}$$

from eqn. 17. Thus t_ν is determined by

$$t_\nu p = sq + \nu \quad , \quad s \in \mathbb{Z} \ , \ |t_\nu| < q \ . \tag{20}$$

Again, there is a mod q ambiguity because of the sign indeterminancy of t_ν. For square lattice, the heuristic of using the smaller $|t_\nu|$ still seems to hold, *e.g.* while both $(t_3, s) = (1, 0)$ and $(t_3, s) = (-6, -3)$ satisfy eqn. 20, the actual system picks $t_3 = 1$. Ref. 20 mentioned that s and t_ν cannot simultaneously be odd for either the hexagonal or triangular lattices. Incidentally, for $\nu = p$, $t_p = 1$ is always a solution with the corresponding $s = 0$, *i.e.* the total Chern number of the lowest p bands is always 1.

Eqn. 20 is the TKNN Diophantine equation[1] for $r = \nu$. There, t_ν is the total Hall conductivity (the sum of the Chern numbers) of the ν occupied bands. It is also the winding number of the energy edge states in the ν^{th} gap[3]. We now have a third interpretation: it is the number of sites traversed by the mobile packet during each κ increment. Equivalently, it is the number of mobile packets transported across any magnetic unit cell boundary during the cycle $k_x \to k_x + 2\pi$.

The entanglement spectrum can now be understood intuitively. Whenever the mobile packet leaves the lower half-cylinder through the cut between M and $M + 1$ (in Fig. 6, proceeding from top-left quadrant through the red line into the lower-right quadrant), there is an occupancy flow from $f = 1$ to 0. The number of flow lines is then equal to the number of packets which move through the cut, which is the total Chern number. In the periodic y boundary case, where the cylinder is compactified into a torus, the flow across $M = N_y/2$, is always concomitant with another packet moving from $y = N_y$ to $y = 1$, hence a symmetric flow from 0 to 1 with its wavefunction localized at the opposite end. (Entanglement occupancy with periodic y boundary is shown in Fig. 8 in the next section). Furthermore, If we change the position of the entanglement cut M (not necessarily along a magnetic cell boundary, for example), this will simply change the value of k_x when a packet hits the cut, whence the k_x translation shown in Figs. 1 and 2.

While the entanglement spectrum only reveals the total Chern number, the correlation matrix retains some information about the individual Chern numbers of constituent bands, manifested as the separation between its wavepackets. Note that eqn. 18 can be taken as a definition of t_ν with arbitrary $\nu < q$, without interpreting ν as the number of filled bands. After all, the total Chern number of the lowest ν bands is the same whether or not they are filled. We explicitly replace ν with $n < q$ below to avoid any such connotation. From eqn. 17 and 18, we have

$$m_{n+1}(\kappa) - m_n(\kappa) = t_{n-1} - t_n = -C_n \ , \tag{21}$$

thus the two packets at m_{n+1} and m_n are separated by a distance of C_n. Quantities such as the four-point correlation $\mathcal{F}(\Delta) = \langle\, c_y^\dagger \, c_y \, c_{y+\Delta}^\dagger \, c_{y+\Delta} \,\rangle$ thus have peaks at $\Delta = C_i$ apart from $\Delta = q$, $2q$, *etc.*

On a square lattice, the Hofstadter model exhibits a particle-hole symmetry. This implies that $C_j = C_{q+1-j}$. For even q, the bulk spectrum is known to have no central gap[21,22], therefore the Chern numbers of the two central bands are not individually well defined, and one can speak only of a Chern number for the pair. It is interesting to notice its implication on the distribution of the wavepackets within each unit cell: if on the contrary there is a central gap, then $t_{q/2} = C_1 + C_2 + \ldots + C_{q/2} = C_q + C_{q-1} + \cdots C_{q/2+1}$. Since the total Chern number of all bands must be zero, we must have $t_{q/2} = 0$. Now according to eqn. 17 and 18, $m_{q/2+1}(\kappa) = m_1(\kappa) - t_{q/2} = m_1(\kappa)$, so the $(\frac{q}{2}+1)^{\text{th}}$ packet and the first one are forced onto the same site. Thus, the fact that there is *no* central gap in this case guarantees that there will be no packet 'collisions'.

The natural question to ask next is how the wave packets are arranged when $\nu > q/2$. To illustrate this, consider a specific case with $p/q = 5/8$ and $\nu = 7$ filled bands. The Chern numbers of the lowest three bands are -3, 5, and -3, respectively, and particle-hole symmetry guarantees that these values repeat for the upper three bands. The central two bands therefore have a combined Chern number of $C_{4,5} = 2$. Since Chern numbers represent the separation between wave packets, we can fill in the first four packets with no difficulty (the position

of the first packet being arbitrary). The location of the fifth packet cannot be determined because C_4 is not well-defined, but the location of the sixth packet is found by shifting the fourth one by $C_{4,5} = 2$. The rest of the packets can be filled in a similar fashion. Thus the vanishing of the central gap implies an indeterminacy of the position of the $(\frac{q}{2}+1)^{\text{th}}$ wavepacket. To resolve this, one can add in an infinitesimal second-neighbor hopping that breaks the particle-hole symmetry and results in a small central gap. For example, one can introduce a second-neighbor hopping t' along one of the two diagonals in each unit cell (say in the direction $\hat{x}-\hat{y}$). This construction interpolates between the square lattice when $t'=0$, and the triangular lattice when $t'=1$ (see Appendix B). For $t' \ll 1$, we find that the Chern numbers of the central two bands are resolved as $C_4 = 5$ and $C_5 = -3$. C_4 can now be used to determine the position of the fifth packet.

4. WANNIER CENTER FLOW

The Diophantine equation (20) describes a mod-q property of the Hofstadter problem, which is a result of the (k_x, y) covariance of eqn. 12. No knowledge of intermediate values of $k_x \in [\,\kappa\phi\,,\,(\kappa+1)\phi\,]$ is required in obtaining eqn. 20. This comes at a price of the ambiguity in t (mod q) and s (mod p), which intuitively contain the information of the direction in which any given packet is moving. In this section, we settle this issue by examining the localized eigenstates of the projectors over the full range of k_x, *i.e.* the Wannier functions.

4.1. Wannier functions in 1D

The application of Wannier functions to the analysis of topological band structures has recently been developed in refs. 14, 15, and 23. Following these references, consider first a periodic one-dimensional system consisting of N unit cells with q internal degrees of freedom per cell. Let X be a cell coordinate and let m index the internal degree of freedom; we may take $X \in \{1,\ldots,N\}$ and $m \in \{1,\ldots,q\}$. Bloch's theorem says $\Psi_{n,k}(X,m) = e^{ikX}\,u_{n,k}(m)$, where n labels the q bands. One may thus decompose the Hilbert space as $\mathcal{H} = \mathcal{H}_X \otimes \mathcal{H}_m$, writing $|\Psi_{n,k}\rangle = |k\rangle \otimes |u_{n,k}\rangle$. Here $|u_{n,k}\rangle$ is an eigenstate of the Fourier transform $H_{mm'}(k)$ of $H_{mm'}(X-X') \equiv \langle X,m\,|\hat{H}|\,X',m'\rangle$, *i.e.* it is a Bloch cell function.

For a system with periodic boundary conditions, the position operator can be taken to be $U = e^{2\pi i\hat{X}/N}$, as in the work of Yu *et al.*[15] An eigenstate of $\widetilde{U} \equiv PUP$, where P is a projector onto a subset of energy bands, is of the form

$$|\Phi_\lambda\rangle = \sum_{n,k} \Phi^\lambda_{n,k}\,|k\rangle \otimes |u_{n,k}\rangle\ , \tag{22}$$

where the sum on the band index n is over the desired subset, and λ labels the eigenvalues. Demanding $\widetilde{U}\,|\Phi_\lambda\rangle = e^{2\pi i\lambda/N}|\Phi_\lambda\rangle$, one obtains $\Phi^\lambda_{m,k+\Delta k} = e^{-2\pi i\lambda/N}\,M_{mn}(k+\frac{1}{2}\Delta k)\,\Phi^\lambda_{n,k}$ (sum on n over selected bands), where

$$M_{mn}(k) = \langle\, u_{m,k+\frac{1}{2}\Delta k}\,|\,u_{n,k-\frac{1}{2}\Delta k}\,\rangle\ , \tag{23}$$

with $\Delta k = 2\pi/N$. The eigenvalue equation, which follows from setting $\Phi^\lambda_{n,0} = \Phi^\lambda_{n,2\pi}$, is then

$$\mathsf{det}\big(e^{2\pi i\lambda} - W\big) = 0\ , \tag{24}$$

where $W = M(N\Delta k - \frac{1}{2}\Delta k)\cdots M(\Delta k - \frac{1}{2}\Delta k)$ is a Wilson loop. Note that λ is not necessarily real since $\widetilde{U}$ is the *projection* of a unitary operator but is not unitary itself. In a more general setting, where the wavefunctions u_m depend on a set of parameters $\vec{g}$, one has

$$\begin{aligned}&\big\langle u_m(\vec{g}+\tfrac{1}{2}\Delta\vec{g})\,\big|\,u_n(\vec{g}-\tfrac{1}{2}\Delta\vec{g})\big\rangle \\ &\quad= \Big[\exp\big(iA^\mu\Delta g_\mu - \tfrac{1}{2}Q^{\mu\nu}\Delta g_\mu\,\Delta g_\nu + \mathcal{O}(\Delta g^3)\big)\Big]_{mn}\ ,\end{aligned} \tag{25}$$

where A^μ is the nonabelian Berry connection,

$$A^\mu_{mn}(\vec{g}) = i\left\langle u_m\,\middle|\,\frac{\partial u_n}{\partial g_\mu}\right\rangle \tag{26}$$

and $Q^{\mu\nu}$ is the quantum geometric tensor[24,25],

$$Q^{\mu\nu}_{mn}(\vec{g}) = \left\langle \frac{\partial u_m}{\partial g_\mu}\,\middle|\,(1-P)\,\middle|\,\frac{\partial u_n}{\partial g_\nu}\right\rangle\ . \tag{27}$$

In our case, as $N\to\infty$ we have that the Wilson loop becomes unitary, and each eigenvalue λ is real.

For a single band, we can write

$$\lambda_I = \int_0^{2\pi}\frac{dk}{2\pi}\,A(k) + I\ , \tag{28}$$

where I is an integer and $A(k) = i\,\langle\,u(k)\,|\,\frac{\partial}{\partial k}\,|\,u(k)\,\rangle$. Thus for a single band, the state $|\Phi_{\lambda_I}\rangle$ is localized at unit cell I with an offset $\gamma/2\pi = \int_0^{2\pi} dk\,A(k)$.

When the internal space of $|u_{n,k}\rangle$ coincides with real space (*e.g.* the lattice site m within the magnetic unit cell in Hofstadter problem), one may refine the definition of the position operator, writing

$$U \to e^{2\pi i\hat{X}/N}\,e^{2\pi i\hat{m}/qN}\ , \tag{29}$$

where $\hat{m} = \sum_{m=1}^{q} m\,|m\rangle\langle m|$ measures the position within each unit cell. For the single band case, this shifts the offsets γ to

$$\tilde{\gamma} = \gamma + q^{-1}\int_0^{2\pi} dk\ \langle u_{n,k}|\,\hat{m}\,|u_{n,k}\rangle\ . \tag{30}$$

Equivalently, one may also introduce the modified cell functions $|\tilde{u}_{n,k}\rangle$,

$$|\tilde{u}_{n,k}\rangle = q^{-1/2} \sum_{m=1}^{q} \langle m \,|\, u_{n,k}\rangle \, e^{-ikm/q} \, |m\rangle \tag{31}$$

and use them in computing the Berry connection.

When the projector P is onto multiple bands, the Wilson loop becomes a matrix, and the eigenvalues of $\widetilde{U}$ are $e^{2\pi i \lambda_{I,w}/N}$, where w is an additional label running from one to the number of bands, *i.e.* the dimension of the projector[23]. One then has

$$\lambda_{w,I} = I + \frac{\theta_w}{2\pi} \ . \tag{32}$$

Again, for systems where the internal 'orbital space' corresponds to real space, one can refine the position operator as in eqn. 29.

For two-dimensional lattices, Wannier functions can be defined at each k_x. For a single band n, its y-center is the Berry phase $\gamma_n(k_x)/2\pi$. The band Chern number is the negative of the winding number of $\gamma_n(k_x)$ over the interval $k_x \in [0, 2\pi]$:

$$\begin{aligned} C_n &= \tfrac{1}{2\pi i} \int\limits_{\rm BZ} d^2k \, \vec{\nabla}_{\vec{k}} \times \langle \psi_n(\vec{k}) | \, \vec{\nabla}_{\vec{k}} \, | \psi_n(\vec{k}) \rangle \cdot \hat{z} \\ &= \frac{\gamma_n(0) - \gamma_n(2\pi)}{2\pi} \ . \end{aligned} \tag{33}$$

Thus the Wannier center shifts by $-C_n$ (magnetic) unit cells over $k_x \to k_x + 2\pi$, as found by Qi in ref. 23. We have seen in §3 that the packet associated with band n is translated by $-C_n$ lattice sites during $k_x \to k_x + 2\pi/q$, so over $k_x \to k_x + 2\pi$, it will be translated by $-C_n$ magnetic unit cells, in agreement with the Wannier picture.

For multiple bands, we have

$$\det W = \exp\left\{ i \int\limits_0^{2\pi} dk \ {\rm Tr}\, A(k) \right\} \tag{34}$$

hence

$$\sum_{w=1}^{\nu} \theta_w = \sum_{n=1}^{\nu} \gamma_n \ , \tag{35}$$

where $\nu = \mathsf{rank}(P)$. Then similar to the single band case, we conclude that in 2D, the total shift of all (inequivalent) Wannier centers is given by the sum of the Chern numbers. This is reflected in §3 as the number of mobile packets transported through any given magnetic unit cell boundary.

When there is no level crossing among $\{\lambda_{w,I}\}$ over the period of k_x, one can combine the w and I indices. Define a composite index $\mu(w, I) = w + \nu I$, with $\lambda_{w,I} \to \lambda_\mu$. Sending k_x from 0 to 2π amounts to an index shift, which is universal for all θ_μ since there is no level crossing. Then the eigenfunctions $\Theta_\mu(k_x)$ of W (here taken to be periodic in the index *modulo* q) satisfy

$$\Theta_\mu(2\pi) = \Theta_{\mu+\sigma}(0) \quad , \quad \sigma \in \mathbb{Z} \tag{36}$$

which is just a cyclic permutation in the w index with an offset σ. One may think of the set of $\{e^{i\theta_w}\}$ as ν points on the unit circle where different indices I are equivalent. Then during the σ cyclic permutation, the perimeter of the circle is covered by these ν points for σ times, *i.e.*,

$$\frac{1}{2\pi} \sum_{w=1}^{\nu} \big[\theta_{w,I}(2\pi) - \theta_{w,I}(0) \big] = \sigma \ . \tag{37}$$

But according to eqn. 35, the LHS is simply the total Chern number of constituent bands,

$$\sigma = -\sum_{n=1}^{\nu} C_n \ . \tag{38}$$

4.2. Wannier center flow in Hofstadter problem and a general relation with the entanglement spectrum

For the Hofstadter model, we have numerically diagonalized the operator $\widetilde{U} = P \, e^{2\pi i \hat{Y}/N_y} \, e^{2\pi i \hat{m}/qN_y} P$, where $Y \in \{1, \ldots, N_y\}$ runs over the unit cells, and $m \in \{1, \ldots, q\}$ runs over the individual sites within each unit cell. States with zero eigenvalues are those projected out by P. For a single band, $P = B_n$, while $P = \mathcal{G}_\nu$ for ν filled bands. We write $\widetilde{U} \, |\theta\rangle = e^{i\theta} \, |\, \theta \,\rangle$, and we compute three slightly different Wannier centers: $y_\theta \equiv \theta N_y/2\pi$, $\langle Y \rangle_\theta \equiv \langle \, \theta \,|\, \hat{Y} \,|\, \theta \,\rangle$, and $\langle y \rangle_\theta \equiv \langle \, \theta \,|\, \hat{Y} + \frac{\hat{m}}{q} \,|\, \theta \,\rangle$, where θ is wrapped in such a way that y_θ is restricted to $[0.5, N_y + 0.5]$. The top panel of fig. 8(a) shows the Wannier centers defined above for the lowest band of $p/q = 3/7$ with $N_y = 28$. The y_θ values, shown as colored dots, have a proper translational property: these values are generated by shifting any single flow by successive multiples of q. In the vicinity of half-odd-integer κ, a Wannier center migrates from one site to the next one which is $-C_1 = 2$ sites ahead. In terms of the corresponding wavefunction (not plotted), what happens is that around integer κ, it has a single peak at the site given by its (rounded) eigenvalue y_θ. As κ slowly moves toward the next half-odd-integer value, some weight is transferred to the next site, causing the eigenvalue y_θ to interpolate between the two values. As k_x is increased by 2π, q such migrations are made, *i.e.*, each Wannier center is shifted backwards by C_1 magnetic unit cells. In the bulk, $\langle y \rangle_\theta$ (colored lines in (a)) and y_θ overlap. Near $y = N_y$, part of the weight is pushed over the boundary to the $y = 1$ end, thus $\langle y \rangle_\theta$ starts to deviate from y_θ and drops, until all weight is transferred to the other boundary.

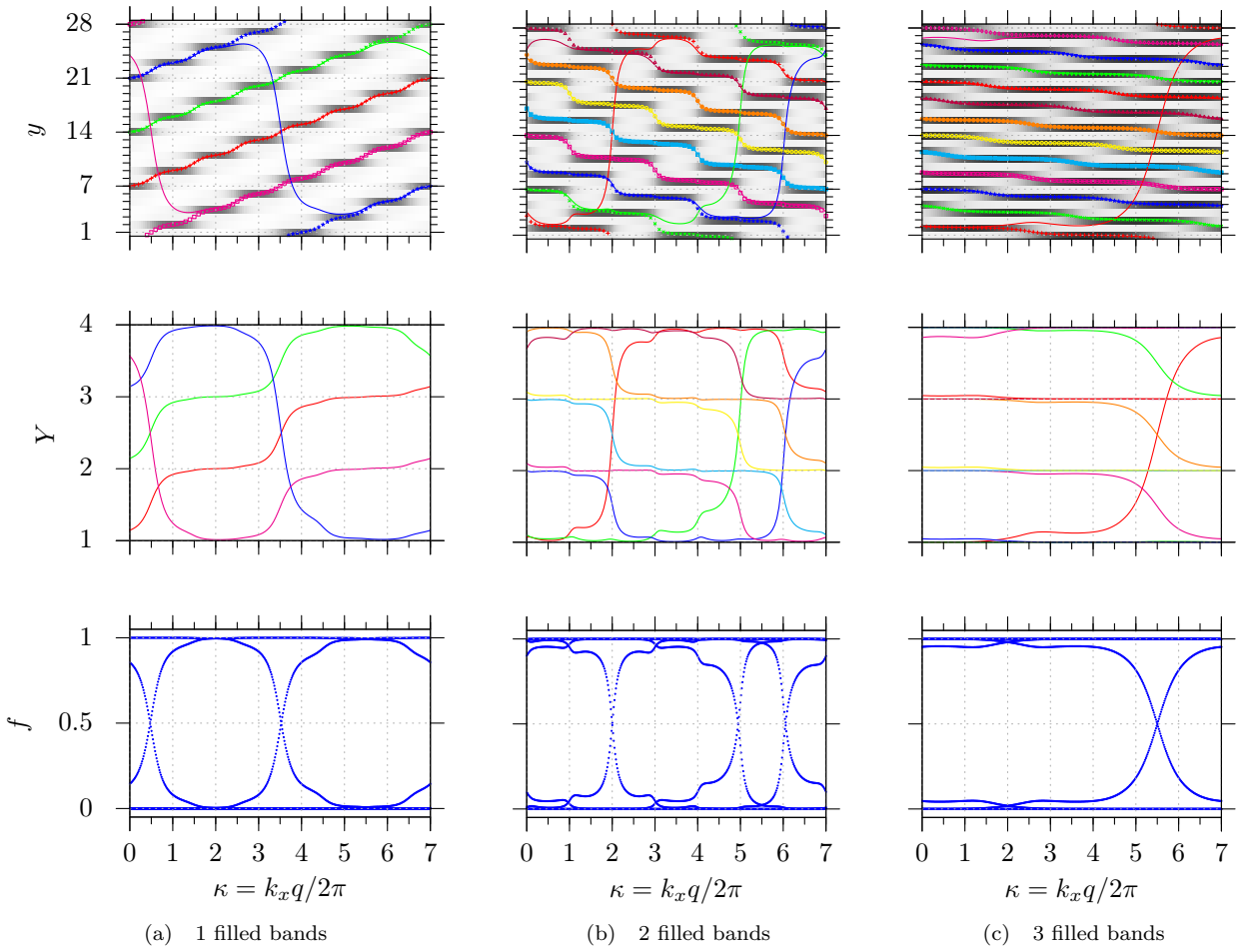

FIG. 8: (Color online) Wannier centers *vs.* entanglement occupancy for $p/q = 3/7$ with different filling fraction and 4 magnetic unit cells in the full system and 2 in the half system. Top: Wannier centers using lattice coordinate $\hat{y}$ as position operator. Colored dots: y_θ. Colored lines: $\langle y\rangle_\theta$. Black-white background: diagonal elements of the lowest band projector B_1, black = 1, white = 0. See also Fig. 6. Center: Wannier center using $\langle Y\rangle_\theta$ (magnetic unit cell coordinate). Corresponding levels have the same color as in top panels. Bottom: entanglement occupancy (no type/color coding). In (a), each type/color of point in the top and center panels corresponds to a packet, *i.e.*, related via (k_x, y) covariance, in this case advancing by $p = 3$ in κ as $y \to y + 6$ (equivalent to $y - 1$). In (b) and (c), each type/color of point corresponds to a mobile packet (because they are not related by the (k_x, y) covariance). Specifically, in (b), advancing κ by $p = 3$ does not change y by -1 or 6, and in (c), advancing κ by 1 does not change y by 2 or -5. It is also clear that within each magnetic cell, only one mobile packet moves as $\kappa \to \kappa + 1$, with $\kappa =$ half-odd-integer in (b) and integer in (c). Notice the similarity between the Wannier center flow and the entanglement flow: a packet (a) or mobile packet (b and c) crossing the magnetic cell within the bulk has almost the same shape as the entanglement downflow; while crossing from $y = N_y$ to $y = 1$ has the almost the same shape as the entanglement upflow. The plateau-like feature in the entanglement flow lines can be traced back to the y plot in the top panels as the motion of a (mobile) packet within one magnetic cell.

If instead of $\widetilde{U}$, we were to diagonalize the operator $\widetilde{V} \equiv P\left(\frac{\hat{Y}}{N_y} + \frac{\hat{m}}{qN_y}\right)P$, then the behavior in the bulk will be the same, but near the edge there will be avoided crossings in the Wannier center flow of $\langle y\rangle_\theta$. The flow of the magnetic unit cell coordinate $\langle Y\rangle_\theta$, shown as colored lines in fig. 8(b), is similar to that of $\langle y\rangle_\theta$, but with an emphasis on the occasions when $\langle y\rangle_\theta$ crosses a magnetic cell boundary.

The Wannier centers of two and three filled bands are shown in Fig. 8. As κ increases by 1, only one Wannier center per magnetic unit cell flows by $\sigma = -\sum_{i=1}^{\nu} C_i$ sites (Eq. 38), corresponding to the motion of a mobile packet in §3. $\sigma = -3$ for two filled bands and 1 for three filled bands. There is no level crossing in y_θ, hence eqn. 38 holds true: following any flow line from $k_x = 0$ to 2π leads one to $-\sigma$ levels beneath the starting point. Notice the same behavior in the entanglement quasienergy of Fig. 4(a).

There is a striking similarity between the magnetic cell coordinate flow $\langle Y\rangle$ and the entanglement occupancy

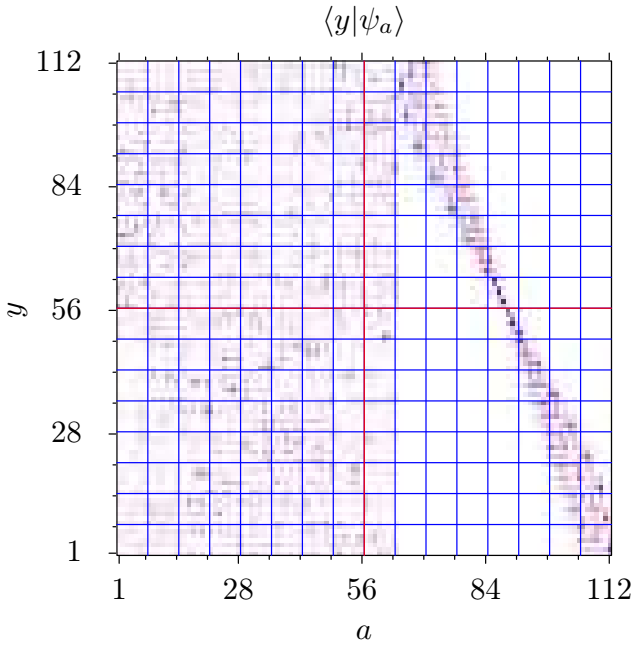

FIG. 9: (Color online) Normalized eigenfunctions $\psi_a(y)$ of $\mathcal{G}R\mathcal{G}$ for $p/q = 3/7$, $N_y = 112$, $M = 56$, and $\nu = 3$ at $k_x = 2\pi/7$ (cylindrical boundary conditions). The Chern number of the filled bands is $C_{\rm occ} = 1$. Color corresponds to the sign of the wavefunction (red for positive, blue for negative), and intensity to amplitude (white for zero intensity).

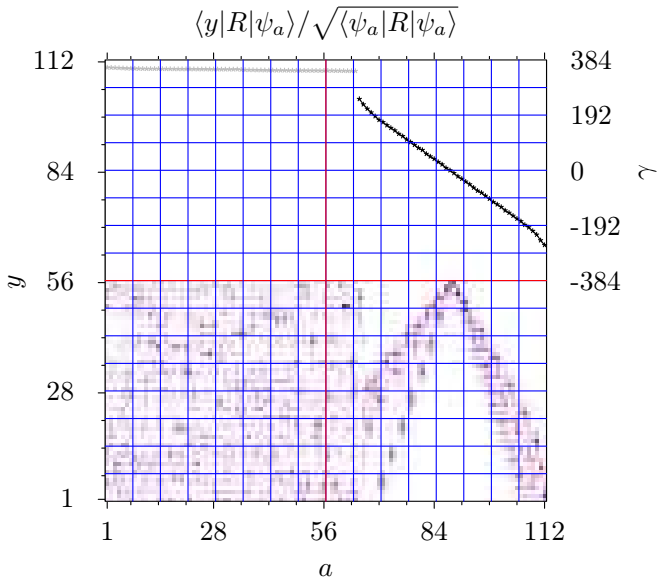

FIG. 10: (Color online) Normalized eigenfunctions $\tilde{\psi}_a(y)$ of $R\mathcal{G}R$ for the parameters given in the caption to Fig. 9. The entanglement energies are plotted in the top half. Grey points correspond to $\gamma_a = \infty$ ($f_a = 0$). As expected, states with entanglement energy $\gamma_a \approx 0$ are localized in the vicinity of the cut.

spectrum, shown in the center and bottom rows of Fig. 8: the upward flow of $\langle Y\rangle$ looks exactly like the upward flow of f, while the downward flow of $\langle Y\rangle$ within each $Y \to Y-1$ sector looks like the downward flow of f. This can be understood in the following way: the spectrum of $\hat{Y}$ can be thought of as a coarse-grained version of $\hat{y}$, and should look just like $\langle Y\rangle$ and $\langle y\rangle$ shown in Fig. 8, so the effect of coarse-graining is to suppress the flow within a coarse-grained cell, and enhance the flow migrating between different cells. One may push the coarse graining to the extreme where all sites with $y \le M$ count as $\bar{y} = 0$, and all above M as $\bar{y} = 1$. Then the only significant flow is from $\bar{y} = 0$ to 1, corresponding to $Y = 2$ to $Y = 3$ in Fig. 8, and from $\bar{y} = 1$ to $\bar{y} = 0$, corresponding to $Y = 4$ through the periodic boundary to $Y = 1$. In Fig. 8, such a coarse graining would keep the upward Y flow intact, while push $Y = 3$ and $Y = 2$ lines to top and bottom respectively for the downward flow, making it look just like the entanglement occupancy spectrum. In fact, one can prove that the coarse-grained Wannier spectrum is *identical* to the entanglement spectrum: Consider two arbitrary projectors P and R. One can think of them as two matrices of the same dimension (zero-padded, if necessary, to fill out the dimensions). We claim that PRP and RPR have identical eigenspectra. To see this, assume $|\psi_a\rangle$ is an eigenstate of PRP with non-zero eigenvalue λ_a. Then

$$|\psi_a\rangle = \tfrac{1}{\lambda_a} PRP\,|\psi_a\rangle \tag{39}$$

and therefore $P|\psi_a\rangle = |\psi_a\rangle$. Thus, $|\psi_a\rangle$ is an eigenstate of P with eigenvalue 1. It then follows that

$$RPR\,|\psi_a\rangle = \lambda_a R\,|\psi_a\rangle\ , \tag{40}$$

from which it follows (using $R^2 = R$) that $|\tilde{\psi}_a\rangle = R\,|\psi_a\rangle$ is an eigenstate of RPR with the same eigenvalue λ_a. Thus the non-zero spectrum of PRP belongs in that of RPR, and vice versa, so they are identical. Since the coarse-grained position operator R is (the complement of) the projector used in constructing the restricted correlation matrix G, the entanglement spectrum of $G = R\mathcal{G}R$ is identical to the coarse-grained Wannier centers $\mathcal{G}R\mathcal{G}$, and the entanglement eigenstates are obtained by projecting the coarse-grained Wannier states onto the relevant half space.

In Fig. 9 we plot the normalized eigenfunctions $\psi_a(y)$ of $\mathcal{G}R\mathcal{G}$ for the case $p/q = 3/7$, $N_y = 112$, $M = 56$, and $\nu = 3$ at $k_x = 2\pi/7$. Note how the behavior of the eigenfunctions mimics that of the Wannier states, with $\psi_a(y)$ localized at a position which moves across the entire cylinder as the label a advances through a range corresponding to the rank of $\mathcal{G}R\mathcal{G}$ ($\frac{3}{7}\times 112 = 48$ in this case; see §2.2.2). States #1 through #64 belong to the kernel of $\mathcal{G}R\mathcal{G}$ and are all degenerate. The insertion of the real space projector R thus fails to resolve these wavefunctions in real space, which explains the speckled pattern

on the left side of the figure. The Wannier states are better localized however, since R may be considered a coarse-grained approximation to y.

In Fig. 10, we plot the normalized eigenfunctions $\tilde{\psi}_a(y)$ of $R\mathcal{G}R$ for the same parameters, along with the corresponding entanglement energies γ_a. (If we remove the upper half of the cylinder, where the wavefunctions vanish, this is a repeat of Fig. 5.) According to our definitions,

$$|\tilde{\psi}_a\rangle = R\,|\psi_a\rangle \Big/ \sqrt{\langle\psi_a|\,R\,|\psi_a\rangle}\ . \tag{41}$$

Note how states of large positive γ_a ($f_a \approx 0$) as well as states of large negative γ_a ($f_a \approx 1$) are localized far from the A/B boundary.

5. SUMMARY

We have studied the entanglement spectrum and Wannier center flows of the Hofstadter problem. Most of the data presented in this paper was for the square lattice with $p/q = 3/7$ flux quanta per unit cell, but most of our observations are robust with respect to changing lattices, fluxes, and fillings. The entanglement spectrum of a subsystem exhibits spectral flow similar to that of the full system's energy edge modes: the total Chern number controls the number of flow lines, and its sign tells the direction of the flow. When cylindrical boundary conditions are used in the full system, the entanglement spectrum exhibits level index discontinuity on the flow line. This is a manifestation of the crossing of the Fermi energy with the full system edge modes, which results in a total occupancy discontinuity. Changing the location of the entanglement cut shifts the entanglement spectrum. This reflects the k_x y covariance of the Hamiltonian: changing k_x to $k_x + 2\pi p/q$ is equivalent to shifting the system in y by $\Delta y = 1$.

The behavior of the entanglement spectrum can be understood by looking at the full system band projectors. These projectors are well localized and thus represented by wavepackets on their diagonals. For single bands, the packets flow under k_x pumping. The (k_x, y) covariance then imposes restrictions on possible flow rate, described by a Diophantine equation first derived by TKNN[1]. Since the Chern numbers are also given by the same equation, the topological property of the system can be described equivalently in terms of the motion of these packets: the number of magnetic unit cells traversed by each packet during one period of k_x is given by the Chern number, with the direction given by its sign. For multiple bands, the flow is that of the mobile packets moving under k_x pumping, and the number of mobile packets crossing a given boundary gives the total Chern number of filled bands. The entanglement spectrum can then be understood as a measure of detecting when these packets cross a particular boundary, namely the entanglement cut.

Using the (k_x, y) covariance alone (and hence the Diophantine equations) only fixes the flow and the Chern numbers up to mod q because it only relates different k_x points of fixed separation of $2\pi/q$. The localization of the projectors suggests the use of Wannier functions for smooth interpolation between these k_x points. For single bands, the Wannier center at each k_x is given by the corresponding Berry phase and is represented by one packet in the projector diagonal. The flow of the Wannier center is then described by the winding number of this Berry phase, which is the band Chern number. For multiple bands, the Berry phase is replaced by a set of eigenvalues of the Wilson loop operator. If there is no level crossing over the full range of k_x, then all levels experience a universal index bump of σ as $k_x \to k_x + 2\pi$, and σ is given by the sum of Chern numbers. In computing the Wannier center, the position operator can be either the (magnetic) unit cell coordinate alone, or one that also includes the internal coordinates (lattice cell within each magnetic cell). The spectrum of the former is a coarse-grained version of the latter. One can take the coarse graining to the extreme of a bipartition, at which point the position operator becomes a real space projector, and the coarse-grained Wannier spectrum becomes identical to the entanglement occupancy spectrum.

6. ACKNOWLEDGMENTS

This work was supported by the NSF through grant DMR-1007028. We thank B. A. Bernevig and A. Alexandradinata for useful discussions, and for comments after reading a draft of this paper.

Appendix A: Incommensurate edge spectrum

Here we first briefly review the edge spectrum with commensurate N_y and q as studied in ref. 3, and then extend its argument to the incommensurate case.

1. Review of commensurate edge spectrum

The Schrödinger equation corresponding to the matrix equation $H(k_x)_{yy'}\psi_{y'} = \varepsilon\psi_y$ is

$$-\psi_{y-1} - \psi_{y+1} - 2\cos(k_x + y\phi)\,\psi_y = \varepsilon\psi_y \tag{A1}$$

cast into transfer matrix form, we have

$$\begin{pmatrix}\psi_{y+1}\\ \psi_y\end{pmatrix} = M_y \begin{pmatrix}\psi_y\\ \psi_{y-1}\end{pmatrix}, \tag{A2}$$

$$M_y = \begin{pmatrix}-\varepsilon - 2\cos(k_x + y\phi) & -1\\ 1 & 0\end{pmatrix} \tag{A3}$$

Notice that M_y depends on ε. The following boundary condition is required for eqn. A2 to also cover the cases of $y = 1$ and N_y,

$$\psi_0 = \psi_{N_y+1} = 0\ . \tag{A4}$$

Then

$$\begin{pmatrix}\psi_{N_y+2}\\ \psi_{N_y+1}\end{pmatrix} = \mathcal{M}_{N_y+1}\begin{pmatrix}\psi_1\\ \psi_0\end{pmatrix} \tag{A5}$$

$$\mathcal{M}_y \equiv M_y M_{y-1}\cdots M_1 \tag{A6}$$

and eqn. A4 implies M_{N_y+1} is a triangular matrix,

$$\left[\mathcal{M}_{N_y+1}\right]_{21} = 0 \tag{A7}$$

The spectrum $\{\varepsilon\}$ consists of all energies satisfying eqn. A7.

Notice that $M_{y+q} = M_y$, so when $N_y + 1 = qL$ with integer L ("commensurate"),

$$\mathcal{M}_{N_y+1} = \mathcal{Q}^L \quad , \quad \mathcal{Q} \equiv \mathcal{M}_q \tag{A8}$$

Now, products of up-triangular matrices are still up-triangular, so eqn. A7 is satisfied if $\mathcal{Q}$ is up-triangular,

$$\mathcal{Q}_{21} = 0 \tag{A9}$$

It is then easy to verify that

$$\psi_{\ell q+1} = \left[\mathcal{Q}_{11}\right]^\ell \psi_1, \quad \psi_{\ell q} = 0 \tag{A10}$$

where $\ell = 1, 2, \ldots, L$, hence the solution is an edge state exponentially localized at $y = N_y$ if $|\mathcal{Q}_{11}| > 1$, and at $y = 1$ if $|\mathcal{Q}_{11}| < 1$.

The edge spectrum $\{\varepsilon\}$ satisfying the condition $\mathcal{Q}_{21}(\varepsilon) = 0$ is the same as the *full* spectrum of a $(q-1)\times(q-1)$ system, so numerically the edge spectrum of $H(k_x, N_y = Lq-1, z=0)$ can be solved by diagonalizing its upper-left $(q-1)\times(q-1)$ submatrix.

Note that eqn. A10 implies the edge states, *with* ψ_0 *included*, has a direct product form

$$|\psi\rangle = \begin{pmatrix}\mathcal{Q}_{11}^0\\ \mathcal{Q}_{11}^1\\ \mathcal{Q}_{11}^2\\ \vdots\\ \mathcal{Q}_{11}^{L-1}\end{pmatrix} \otimes \begin{pmatrix}\psi_0\\ \psi_1\\ \psi_2\\ \vdots\\ \psi_{q-1}\end{pmatrix}, \tag{A11}$$

i.e., $\psi_{\ell q+m} = \mathcal{Q}_{11}^\ell \psi_m$ with $\ell = 0, 1, \cdots L-1$ and $m = 0, 1, \cdots q-1$. The N-component magnetic cell part dictates the real-space behavior. In this case it is exponentially localized at either end. The q-component internal part is obtained by prepending $\psi_0 = 0$ to the solutions of the $(q-1)\times(q-1)$ upper-left block of H. This is by no means a general form of edge states, but we do also notice a similar decomposition in the zigzag edge modes of the Haldane model[26]. Note also that all Bloch states have such a decomposition, $|\Psi(k,n)\rangle = |k\rangle \otimes |\psi_n(k)\rangle$ where $\langle y|k\rangle = e^{iky}/\sqrt{N}$ is the Bloch phase and $|\psi_n(k)\rangle$ is the n^{th} band eigenstate of the Fourier transformed $q\times q$ Hamiltonian. One may then say that $-i\log(\mathcal{Q}_{11})$ is the imaginary Bloch vector, and which of the UHP or LHP it resides in tells the localization of the edge states.

2. Incommensurate edge spectrum

In the thermodynamic limit where $N_y \to \infty$, one can extend the commensurate argument to incommensurate cases, $N_y + 1 = Lq + m$, with $m = 0, 1, 2, \ldots, q-1$.

First, we note two properties of the transfer matrix,

$$\det\left(M_y\right) = 1 \tag{A12}$$

$$M_{y+m}(k_x, \varepsilon) = M_y(k_x + m\phi, \varepsilon) \tag{A13}$$

both are straightforward from definition. Eqn. A13 expresses the same $k_x\, y$ covariance as eqn. 15. The $(Lq+m)$-step transfer matrix can then be divided in two ways,

$$\mathcal{M}_{Lq+m}(k_x) = \mathcal{M}_m(k_x)\mathcal{Q}^L(k_x) \tag{A14}$$

$$= \mathcal{Q}^L(k_x + m\phi)\mathcal{M}_m(k_x) \tag{A15}$$

If $\mathcal{Q}(k_x)$ satisfies the commensurate edge condition eqn. A9, then

$$\mathcal{Q}^L(k_x) = \begin{pmatrix}\left[\mathcal{Q}_{11}\right]^L & x\\ 0 & \left[\mathcal{Q}_{22}\right]^L\end{pmatrix}_{k_x}, \tag{A16}$$

where x is some number of no interest. We then have

$$\mathcal{M}_{Lq+m}(k_x) = \underbrace{\begin{pmatrix}A_{11} & A_{12}\\ A_{21} & A_{22}\end{pmatrix}}_{\mathcal{M}_m(k_x)} \begin{pmatrix}\left[\mathcal{Q}_{11}\right]^L & x\\ 0 & \left[\mathcal{Q}_{22}\right]^L\end{pmatrix}_{k_x}, \tag{A17}$$

hence

$$\left[\mathcal{M}_{Lq+m}\right]_{21}(k_x) = A_{21}\left[\mathcal{Q}_{11}\right]^L(k_x) \tag{A18}$$

$$= A_{21}\left[\mathcal{Q}_{22}\right]^{-L}(k_x)$$

where the second equality follows from $\det\mathcal{Q} = 1$, a consequence of eqn. A12.

Similarly, if $\mathcal{Q}(k_x + m\phi)$ satisfies the commensurate edge condition eqn. A9, we have instead

$$\mathcal{M}_{Lq+m}(k_x) = \begin{pmatrix}\left[\mathcal{Q}_{11}\right]^L & x\\ 0 & \left[\mathcal{Q}_{22}\right]^L\end{pmatrix}_{k_x+m\phi} \begin{pmatrix}A_{11} & A_{12}\\ A_{21} & A_{22}\end{pmatrix} \tag{A19}$$

thus

$$\left[\mathcal{M}_{Lq+m}\right]_{21}(k_x) = \left[\mathcal{Q}_{22}\right]^L(k_x + m\phi)A_{21} \tag{A20}$$

$$= \left[\mathcal{Q}_{11}\right]^{-L}(k_x + m\phi)A_{21}$$

We can then conclude that in the limit $L \to \infty$,

1. If (k_x, ε) is a solution of the commensurate case $N_y + 1 = Lq$ at the *lower* edge, $\left[\mathcal{Q}_{11}\right]^L(k_x) \to 0$, then by eqn. A18, it is also a solution of incommensurate $N_y + 1 = Lq + m$. For $y \in [1, Lq-1]$, the wavefunction ψ_y coincides with that of the commensurate case, and in the upper tail where $y = Lq + m$, $\psi_y = A_{11}\left[\mathcal{Q}_{11}\right]^L\psi_1 \to 0$, thus it is also at the lower edge.

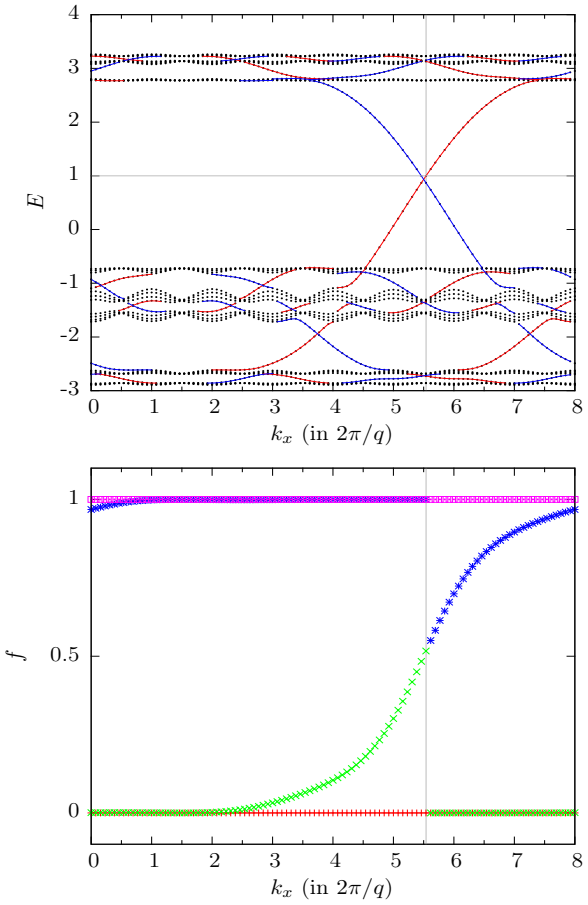

FIG. 11: (Color online) Energy and entanglement spectrum on a triangular lattice with cylindrical boundary condition. Parameters used are $p/q = 5/8$, $N_y = 32$ and $E_\mathsf{F} = 1$. In the energy spectrum (top panel), black dots represent bulk levels, red lines represent edge modes localized along the lower edge ($y = 1$), and blue lines represent those localized along the upper edge ($y = N_y = 32$). Vertical gray line indicates the k_x value at which E_F intersects the lower edge state. The entanglement occupancies (bottom panel) are computed for the lower half of the cylinder ($1 \le y \le 16$), color and symbol-coded according to a. The sudden color change happens when the lower edge mode crosses E_F.

2. If (k_x, ε) is a solution of $N_y + 1 = qL$ at the *upper* edge, $[\mathcal{Q}_{11}]^{-L}(k_x) \to 0$, then by eqn. A20, $(k_x - m\phi, \varepsilon)$ will be a solution of incommensurate $N_y + 1 = Lq + m$. It is also at the upper edge because $\psi_y \to 0$ in the lower tail.

thus for $N_y \to \infty$, an increment of N_y by 1 leaves the lower edge spectrum unchanged, while shifting the upper edge spectrum in k_x by $-2\pi p/q$.

Appendix B: Triangular lattice

The Hofstadter model on a triangular lattice can be obtained by adding in each square plaquette a diagonal bond along the $\hat{x} - \hat{y}$ direction with half-odd-integer vector potential (in units of $\phi = 2\pi p/q$), such that the flux per triangle is $\phi/2$. Instead of eqn. 3, the Hamiltonian matrix is now

$$H(k_x, N_y, z) = -\begin{pmatrix} c_1 & v_1 & 0 & \cdots & z^* v^*_{N_y-1} \\ v_1^* & c_2 & v_2 & & 0 \\ 0 & v_2^* & \ddots & & \vdots \\ \vdots & & & & v_{N_y-1} \\ z v_{N_y} & 0 & \cdots & v^*_{N_y-1} & c_{N_y} \end{pmatrix} \tag{B1}$$

where

$$c_y = 2\cos(k_x + y\phi) \quad , \quad v_y = 1 + t'\, e^{-i(k_x + y\phi + \frac{1}{2}\phi)} \ , \tag{B2}$$

with $t' = 1$ for triangular lattice, and 0 for square lattice. The discussion of edge spectrum in Appendix A remains essentially the same, except the transfer matrix, eqn. A3, now becomes

$$M_y = \begin{pmatrix} -\dfrac{\varepsilon + c_y}{v_y} & -\dfrac{v^*_{y-1}}{v_y} \\ 1 & 0 \end{pmatrix} . \tag{B3}$$

In the pathological case where certain $v_{\tilde{y}} = 0$, the open edge Hamiltonian (*i.e.*, $z = 0$) reduces to two blocks, $\{1, \ldots, \tilde{y}\}$ and $\{\tilde{y} + 1, \ldots, N_y\}$, each of which can be individually solved; alternatively one can shift t slightly away from 1. Note that while $\det M_y$ is no longer one, the q-step transfer matrix $\mathcal{Q}$ still has unimodular determinant,

$$|\det \mathcal{Q}| = \left| \frac{v_0^* v_1^* \cdots v_{q-1}^*}{v_1 v_2 \cdots v_q} \right| = 1 \ , \tag{B4}$$

where we used $v_0 = v_q$. Consequently,

$$|Q_{22}| = |Q_{11}|^{-1} \ , \tag{B5}$$

and eqns. A18 and A20 hold up to a phase. The conclusion thus remains unchanged that lower edge states are unchanged while upper edge states shift in k_x with incommensurate N_y.

In Fig. 11, we plot the cylindrical boundary energy spectrum, and its entanglement spectrum with $\nu = 5$ filled bulk bands for $p/q = 5/8$ on the triangular lattice. The Chern numbers of individual bands are either $C = -3$ or 5, which are equivalent *modulo* $q = 8$, and the lowest band has $C = -3$. Both are in agreement with what we observed in the square lattice case, namely, all band Chern numbers are equivalent *modulo* q, and that the lowest band Chern number is the one with smaller magnitude. The number of edge spectral flows in each gap is the total band Chern number below the gap, and the entanglement spectral flow mimics the behavior of edge spectral flow, and has an index discontinuity at k_x

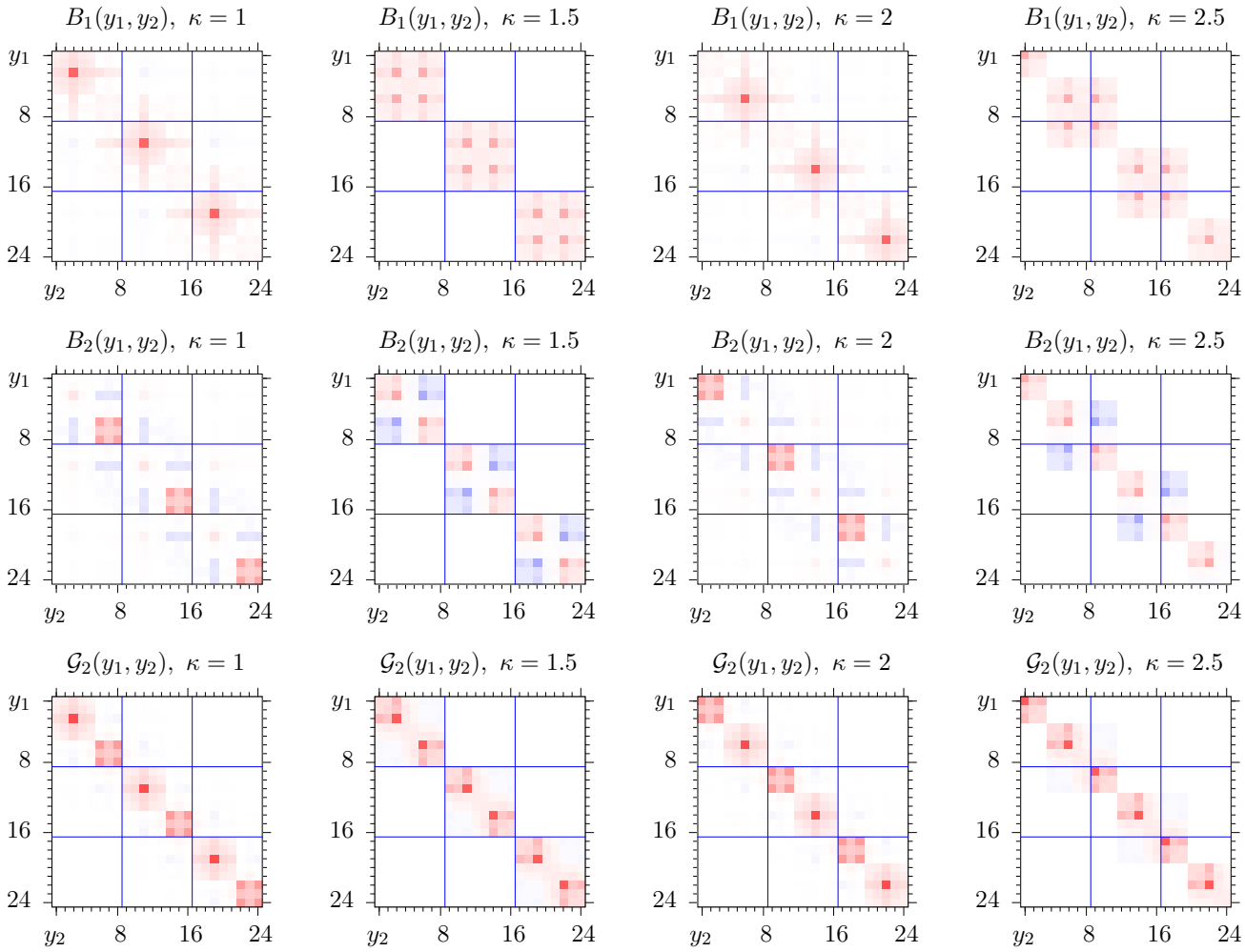

FIG. 12: (Color online) Full system band projectors for $p/q = 5/8$, $N_y = 32$, with periodic boundary conditions in y and $k_x = 2\pi\kappa/q$, B_j and $\mathcal{G}_\nu$ are projectors for the j^{th} band and ν lowest bands, repectively, see also Fig. 6. Here we only plot the 24×24 submatrix belonging to the first three magnetic unit cells. Since the Hamiltonian eqn. B1 can no longer be made purely real, the projectors are in general complex, so we only plot the real part of their matrix elements. Their signs are represented by color, red for positive and blue for negative, and their magnitudes represented by intensity. The individual bands B_1 and B_2 are better localized at $\kappa = 1$ where the gap between them is maximal, while their sum, $\mathcal{G}_2$, is better localized at $\kappa = 1.5$ where the gap between them is minimal. Note that at both κ, the off-diagonal subblocks of both B_j within each 8×8 block tend to cancel (they have different colors). The adiabatic evolution of the wave packets are obvious: for example, at $\kappa = 1.5$, the wave packets of $\mathcal{G}_2$, in each unit cell, are at $y = 3$ and 6 (mod q. Same below). At $\kappa = 2$, the wave packet at $y = 3$ is in the progress of moving toward $y = 1$ while the one at $y = 6$ is "frozen". At $\kappa = 2.5$, the first wave packet arrives at $y = 1$. In the next $\kappa \to \kappa + 1$ sub-cycle, the first wave packet will be frozen and the second one will migrate in the diagonal line by -2 (negative of the total Chern number).

where Fermi energy intersects the lower edge mode. Note that for $\nu = 5$ filled bands, the total Chern number is 1, as reflected in the number of edge and entanglement spectral flows. This agrees with our observation that the total Chern number of p filled bands is one, see discussion following eqn. 20 in the text.

As in the square lattice case, the band projectors and their sums also flow under adiabatic k_x pumping, and the number of wave packets crossing any given boundary during one cycle of the pumping reflects the Chern number of the projectors. Fig. 12 shows the flow of the lowest two band projectors, B_1 and B_2, and their sum $\mathcal{G}_2$, at $k = \kappa \cdot 2\pi/q$ with $\kappa = 1$ and 1.5. Both B_j and $\mathcal{G}_\nu$ have better localization at either integer or half-odd-integer κ where its gap from neighboring bands are maximal.

We thus conclude that the observations as detailed in the text using square lattice are robust and insensitive to the underlying lattice used.

[1] D. J. Thouless, M. Kohmoto, M. P. Nightingale, and M. den Nijs, Phys. Rev. Lett. **49**, 405 (1982).
[2] D. R. Hofstadter, Phys. Rev. B **14**, 2239 (1976).
[3] Y. Hatsugai, Phys. Rev. Lett. **71**, 3697 (1993).
[4] H. Li and F. D. M. Haldane, Phys. Rev. Lett. **101**, 010504 (2008).
[5] F. D. M. Haldane, Bull. Am. Phys. Soc. **54** (2009).
[6] S.-A. Cheong and C. L. Henley, Phys. Rev. B **69**, 075111 (2004).
[7] S.-A. Cheong and C. L. Henley, Phys. Rev. B **69**, 075112 (2004).
[8] I. Peschel, J. Phys. A **36**, L205 (2003).
[9] I. Peschel, J. Stat. Mech. **2004**, P06004 (2004).
[10] A. M. Turner, Y. Zhang, and A. Vishwanath, Phys. Rev. B **82**, 241102 (2010).
[11] T. L. Hughes, E. Prodan, and B. A. Bernevig, Phys. Rev. B **83**, 245132 (2011).
[12] X.-L. Qi, Y.-S. Wu, and S.-C. Zhang, Phys. Rev. B **74**, 045125 (2006).
[13] W. Kohn, Phys. Rev. **115**, 809 (1959).
[14] A. A. Soluyanov and D. Vanderbilt, Phys. Rev. B **83**, 035108 (2011).
[15] R. Yu, X. L. Qi, A. Bernevig, Z. Fang, and X. Dai, Phys. Rev. B **84**, 075119 (2011).
[16] C. Brouder, G. Panati, M. Calandra, C. Mourougane, and N. Marzari, Phys. Rev. Lett. **98**, 046402 (2007).
[17] I. D. Rodríguez and G. Sierra, Phys. Rev. B **80**, 153303 (2009).
[18] A. Alexandradinata, T. L. Hughes, and B. A. Bernevig, Phys. Rev. B **84**, 195103 (2011).
[19] J. D. Cloizeaux, Phys. Rev. **135**, A685 (1964).
[20] D. Thouless, Surface Science **142**, 147 (1984), ISSN 0039-6028.
[21] X. Wen and A. Zee, Nuclear Physics B **316**, 641 (1989), ISSN 0550-3213.
[22] M. Kohmoto, Phys. Rev. B **39**, 11943 (1989).
[23] X.-L. Qi, Phys. Rev. Lett. **107**, 126803 (2011).
[24] J. Provost and G. Vallee, Commun. Math. Phys. **76**, 289 (1980).
[25] L. Campos Venuti and P. Zanardi, Phys. Rev. Lett. **99**, 095701 (2007).
[26] Z. Huang and D. P. Arovas, ArXiv e-prints (2012), 1205.6266.
[27] Since any projector squares to itself, each column is an eigenstate with eigenvalue 1. However, they are not normalized, nor are they orthogonal to each other (because no eigenstate with eigenvalue 0 is present). In fact the construction of Wannier states is one way to orthonormalize these eigenstates.